Computers and Electronics in Agriculture 244 (2026) 111543

Contents lists available at ScienceDirect

Computers and Electronics in Agriculture

journal homepage: www.elsevier.com/locate/compag

Original papers

Comparison of soil property predictions in Lithuanian croplands using UAV, satellite, EMI data and machine learning

R. Žydelis [a,*], L. Weihermüller [b], L.C. Gomes [c], A.B. Møller [c], F. Castaldi [d], J. Volungevičius [a], A. Kavaliauskas [a], T. Koganti [c], J. Wetterlind [e], İ. Cinkaya [f], L. Borůvka [g], F. van Egmond [h], S. Higgins [i], F. Liebisch [j], V. Povilaitis [a], A. Kazlauskaitė-Jadzevičė [a], K. Amalevičiūtė-Volungė [k], S. Pranaitienė [a], E. Vaudour [l]

[a] Institute of Agriculture, Lithuanian Research Centre for Agriculture and Forestry, Lithuania
[b] Agrosphere Institute (IBG-3), Forschungszentrum Jülich GmbH, Germany
[c] Department of Agroecology, Aarhus University, Blichers Allé 20, 8830 Tjele, Denmark
[d] Institute of BioEconomy, National Research Council of Italy (CNR), Via Giovanni Caproni 8, 50145 Firenze, Italy
[e] Swedish University of Agricultural Sciences, Department of Soil and Environment, Skara, Sweden
[f] Ministry of Agriculture and Forestry/General Directorate of Agricultural Research and Policies, Turkey
[g] Czech University of Life Sciences Prague (CZU), Department of Soil Science and Soil Protection, Kamýcká 129, 165 00 Prague-Suchdol, Czech Republic
[h] Wageningen Environmental Research, P.O. Box 47, 6700 AA Wageningen, the Netherlands
[i] Agri-Food and Biosciences Institute, Belfast, Northern Ireland, UK
[j] Agroecology and Environment, Agroscope, Zürich, Switzerland
[k] Lithuanian Agricultural Advisory Service, Akademija, Lithuania
[l] Université Paris-Saclay, INRAE, AgroParisTech, UMR EcoSys, 91120 Palaiseau, France

ARTICLE INFO

Keywords:
Clay
Electrical conductivity
Proximal sensing
Remote sensing
SOC

ABSTRACT

Combining remote and proximal sensing provides a cost-effective solution for mapping soil properties in croplands. This study assessed the potential of remote sensing based on high resolution multispectral UAV imagery (2.6 cm), satellite (Sentinel-2), and in-field measured electromagnetic induction (EMI) data for predicting six soil properties – soil organic carbon content (SOC), clay, sand, silt contents, pH, and soil water content (SWC) – across five Lithuanian agroclimatic zones. Seven modelling scenarios, using individual and combined sources of sensor data, employing a random forest model, were evaluated. To assess real-world applicability, sampling-reduction simulation were additionally performed. SOC and clay predictions achieved the highest accuracy, while silt, sand, and SWC showed acceptable accuracy only in a few sites or specific modelling scenarios. Soil pH predictions were poor across all scenarios. Prediction accuracy varied across study sites, likely influenced by climate, soil parent material, topography, and agricultural management. Sensor data resolutions (2.6 cm, 1.6 m, 10 m per pixel) significantly affected prediction accuracy. For SOC predictions, UAV and Sentinel-2 data performed best, while EMI alone was less effective. In contrast, for clay predictions, EMI data yielded the highest accuracy, emphasizing its role for soil texture assessment. Multi-sensor fusion improved model performance during training but did not consistently enhance validation accuracy across sites, highlighting important cost–accuracy trade-offs and the need for realistic performance evaluation. Overall, the results demonstrate that the benefits of multi-sensor soil mapping are property-specific and site-dependent, providing guidance for scalable and economically viable field-scale soil mapping strategies.

1. Introduction

The vitality of life on Earth depends on soil health, as soils provide 95% of the world's food (EU, 2021). Soils also play a key role in nutrient cycling, carbon storage, and partitioning of surface runoff and water infiltration, which can help mitigate climate change and reduce flooding risks (Adhikari and Hartemink, 2016). Soil health relies on complex interactions between chemical, biological, and physical processes (Vogel

---

* Corresponding author.
E-mail address: renaldas.zydelis@lammc.lt (R. Žydelis).

https://doi.org/10.1016/j.compag.2026.111543
Received 13 November 2025; Received in revised form 19 January 2026; Accepted 5 February 2026

et al., 2018) and represents the soil's ability to respond to external stresses. In agricultural systems, soil health is largely influenced by the agricultural practices, supporting the production of food, fiber, and fodder as well as other essential ecosystem services (Kibblewhite et al., 2007).

Worldwide, the agricultural sector currently undergoes rapid digitalisation and there is an increasing interest in utilizing remote sensing products to determine the soil physical and chemical properties, such as soil organic carbon content (SOC), pH, soil texture, or soil water content (Mendes et al., 2022). Periodic monitoring of important soil health indicators, especially SOC changes, becomes even more relevant for the adaptation or modification of new crop management practices as those recommended by e.g. the Food Safety and Food Security (FAO) program or the European Green Deal (Tziolas et al., 2021). Additionally, the practice of "*Carbon farming*" has become increasingly popular in the agricultural sector over the last years, as it aims to increase carbon storage in the soil to improve soil fertility, while reducing atmospheric carbon dioxide (CO_2) concentrations (Leifeld, 2023). Carbon farming also requires new methods to detect SOC changes in order to efficiently manage and evaluate changes in soil carbon stocks. Soil pH controls the availability of plant nutrients (Hartemink et al., 2023), the clay fraction impacts a wide range of soil physical and chemical processes, while sand and silt are important indicators of soil weathering and soil development processes (William et al., 1991). Soil texture also impacts nutrient availability as well as soil water retention and transmissivity. Therefore, monitoring the current status of the aforementioned soil properties in croplands can support soil fertility assessment, but will also help in decision making for land management or to estimate crop yield potentials (Lamichhane et al., 2019).

Conventional soil surveys with local soil sampling and associated laboratory analysis for quantifying soil properties including SOC content, soil texture, or pH are tedious and labour intensive, and therefore, sampling and analysis is often carried out at a relatively limited number of locations, which might not reflect the natural variability in space and time. In addition, the limited number of samples might fail to meet the criteria for soil quality assessment for precision agriculture or (geo-) statistical methods. Over the past few decades, satellite-derived methods emerged for retrieving spatial information on SOC (Aqdam et al., 2022; Vaudour et al., 2022; Yuzugullu et al., 2024), particularly at local scale (Castaldi et al., 2023), and recently, the bare soil reflectance was incorporated into a Digital Soil Mapping (DSM) framework for SOC estimation (Richer-de-Forges et al., 2023; Urbina-Salazar et al., 2023). The DSM framework introduced by McBratney et al. (2003) evaluated a range of methods for predictive modelling and data acquisition and put forward a methodology for creating digital soil maps. The proposed *scorpan* method includes environmental covariates consisting of soil, vegetation, climate, topography, time and space, which represent the environmental factors affecting the soil (McBratney et al., 2003). In the described workflow, a quantitative connection between observed soil properties and environmental covariates is established in a first step, which is subsequently employed to predict soil properties at an unsampled location. Due to advancements in DSM, the accuracy of SOC prediction has significantly improved over the past few decades for different scales of interest.

Currently, a combination of remote and proximal sensing data with machine learning (ML) algorithms has been proposed to support the characterization of the soil properties and its spatial variability at the field (Benedetto et al., 2022), sub-catchment (Zayani et al., 2023), or even regional scale (Castaldi et al., 2019; Faramarzi et al., 2022). However, the application of remote and proximal sensor data (satellite, unmanned aerial vehicle (UAV), or electromagnetic induction (EMI) measurements) in combination with ML raises several research questions, such as data integration and compatibility, data quality, temporal and spatial resolutions, amongst others. These challenges are particularly relevant for DSM especially in terms of how frequently and effectively soil data are updated, as each of the aforementioned methods has its own advantages and disadvantages. For instance, key advantages of UAVs encompass the relative affordability of the equipment (compared to aircraft), autonomous and simple flight management, the capability for frequent flights, and easy transportation to the site of investigation thanks to their relatively small size and low weight (Mohsan et al., 2022). Additionally, the option to interchange cameras allows for capturing images at higher resolutions. On the other hand, UAVs also have limitations, such as restricted flight duration (typically less than 30 min), an inability to operate under adverse weather conditions (e.g., rain, strong wind, cold conditions), and possible limited payload restricting sensor capability. The effectiveness of UAVs also depends on the time of acquisition during the day and lighting conditions. Primarily, UAVs are best suited for monitoring areas covering less than 70 ha (depending on ground resolution required) and there are specific areas where their operation is prohibited or limited (e.g., areas close to settlements, roads, or critical infrastructure).

In contrast, satellite images can cover large regions, making them suitable for large-scale monitoring, such as at the regional or national-level efforts. Additionally, many satellite products are freely accessible, with periodic updates every $2 - 7$ days, and comprehensive historical data archives are often also available (Segarra et al., 2020). However, there are notable drawbacks such as the unavailability of visible or near-infrared satellite images under cloud or haze cover — a situation particularly pertinent to northern climatic zones (Castaldi, 2021). Furthermore, the spatial resolution of freely available satellite images is often comparatively low (e.g. 10–20 m for Sentinel-2), and the presence of non-soil features (like forests, rivers, buildings, etc.) in close proximity to the area under investigation may disrupt the precision of the data analysis.

Ground-based proximal sensors, such as EMI, are mainly suited for smaller areas, but they provide data with high spatial resolutions, often including information on soil properties for the entire root zone ($1 - 2$-meter depth for most commonly used instruments) (Møller et al., 2021). Additionally, EMI measurements can be obtained under weather conditions which would prevent the use of other sensors, including light rain and overcast skies. However, excessively wet or dry conditions are not ideal for accurate measurements. The primary drawbacks of EMI sensors are the relatively high costs of data acquisition and the need to conduct measurements close to the surface. While they do not require direct contact with the soil, their performance is influenced by the distance between the sensor and the soil surface, which can affect the depth response curve. Additionally, measurements over higher crop stands can be challenging. Finally, additional equipment, such as an All-Terrain Vehicle (ATV), is required to pull the sensor over the area of investigation, which complicates transportation between sites.

The majority of remote-sensing based studies have been conducted across relatively large areas covering more than 100 km^2 (Vaudour et al., 2022). Some studies have even aimed to predict soil properties at fine spatial resolutions (around 10–25 m) over extensive regional areas of more than 1000 km^2 (Castaldi et al., 2019; Žížala et al., 2019; Dvorakova et al., 2023; Urbina-Salazar et al., 2023; Vanongeval et al., 2024). Conventional soil maps at coarse scales frequently fail to account for the intra-field soil variation (Söderström et al., 2016, Brogi et al., 2020), although many studies highlight the importance of these maps for farm applications (Brogi et al., 2021; Han et al., 2022, Wetterlind et al., 2025). In reality, most farmers are not aware of the existence of high-resolution soil maps, not knowing to have access to this information. For regional or national-scale applications (e.g., carbon accounting), the accuracy of the predictions is also unreliable, as stated by Lemercier et al. (2022). Recent reviews by Richer-de-Forges et al. (2023) and Gomes et al. (2023) have analysed the contribution of remote sensing to support DSM. Both studies concluded that this field still faces many challenges which need to be addressed before soil maps based on remote sensing be used by a broad spectrum of stakeholders, including farmers.

In this study, we evaluated the effectiveness of various remote and proximal sensing technologies for mapping SOC, soil texture, pH, and soil water content across five agricultural fields located at different agroclimatic zones in Lithuania.

We hypothesized that the predictive performance would be soil-property specific, with EMI data improving clay and texture predictions due to its sensitivity to subsurface electrical conductivity controlled by clay minerology, while UAV and Sentinel-2 data would better predict SOC owing to their sensitivity to soil organic matter in the visible and near-infrared spectral regions. We further expected that differences in spatial resolution between UAV and satellite data would influence prediction accuracy and scalability for field-level applications. To test these hypotheses, seven modelling scenarios representing all possible combinations of satellite, UAV, and EMI data were evaluated using a machine-learning approach. In addition to assessing prediction accuracy, secondary objectives included evaluating the cost-efficiency of reduced soil sampling strategies and critically assessing the practical feasibility of UAV-based soil mapping compared with freely available satellite data.

This study provides one of the first integrated field-scale assessments of UAV multispectral imagery, Sentinel-2 satellite data, and EMI measurements in the Nordic–Baltic region. By systematically evaluating seven sensor combinations across five contrasting agroclimatic zones, we offer novel insights into soil-property-specific sensor performance, cost–accuracy trade-offs, and the practical feasibility of multi-sensor soil mapping under realistic field conditions. By explicitly addressing both successful and unsuccessful prediction outcomes, the study aims to support informed sensor selection and realistic expectations for operational soil mapping and precision agriculture applications in regions with contrasting pedoclimatic conditions.

2. Materials and methods

2.1. Study area

Lithuania, located in northern Europe, lies on the eastern coast of the Baltic Sea. The total land area is 65,286 km^2, of which 52% is used as cropland, 33% are forests, 6% is classified as other land uses (wetlands, fallow, natural areas), 4% are water bodies, and 5% are urban areas and roads (National Land Service, 2021). The landscape was shaped by the glaciers of the last Ice Age around 10,000 years ago (Basalykas, 2014). According to The Environmental Stratification of Europe, Lithuania is in the nemoral climate zone characterized as continental and cool with a rather short vegetation growing period for crops (Metzger et al., 2012). The southern parts of Estonia, Latvia, and north-western Belarus are also located in this climate zone. Despite the relatively flat topography (average $\approx$ 110 m above sea level), the environmental conditions of the country are non-uniform in terms of air and soil temperatures, precipitation, and soil types. The mean annual air temperature varies between 5.8 and 7.6°C, and annual precipitation between 550 and 910 mm (Kavaliauskas et al., 2023). The main soil types are Luvisols, Cambisols, Gleysols, and Arenosols, covering 29, 16, 15, and 13% of the land area, respectively. According to these pedoclimatic differences, the country can be divided into three main agroclimatic districts, whereby each can be further subdivided into sub-districts (a, b, c, d) (Fig. 1).

2.2. Test sites and soil data

The size of agricultural fields in Lithuania ranges from 0.9 to 263 ha, with an average size of 2.6 ha (National Paying Agency, 2023). Fields with areas of 2 − 5 ha cover approximately 22% of all agricultural land. Therefore, this study concentrates on predicting soil properties at the local scale in agricultural fields, targeting fields with sizes between 2

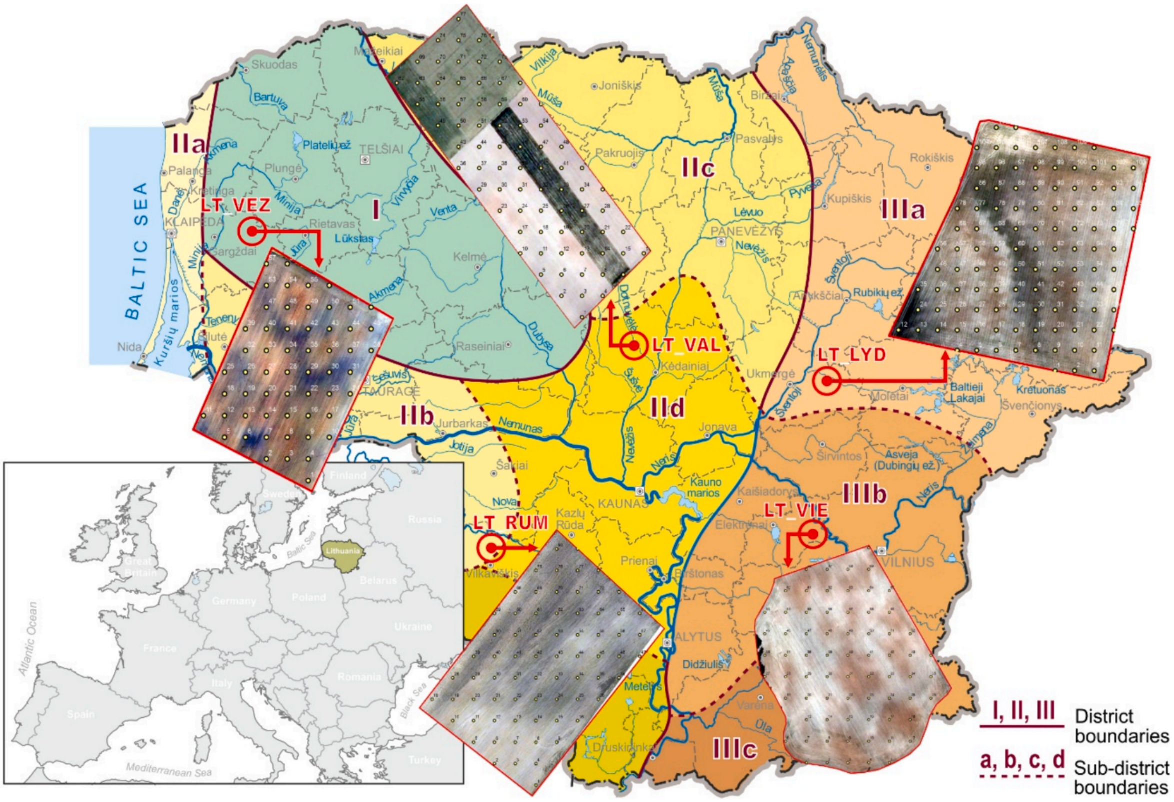

Fig. 1. Lithuanian agroclimatic zones and geographical locations of the five selected sites used in this study for the estimation of soil organic carbon content, soil texture, pH, and soil water content. The numbers (I, II, III) and the letters (a, b, c, d) denote districts and sub-districts of the agroclimatic zones, respectively (Bukantis, 2009).

and 5 ha.

The five agricultural sites selected for this study (Fig. 1) cover the diversity of Lithuanian agroclimatic conditions and soil types as well as different farming systems. The fields have comparable sizes, ranging from 2.3 to 4.7 ha, with mean sampling densities of 24 − 26 ground truth samples per ha. Soil sampling and UAV data were collected at the same date and within a couple of days for the satellite data (Table 1). In three fields, soil sampling was conducted before sowing spring crops, i.e., in early spring 2021. Specifically, following soil sampling, sugar beet was sown in the LT_RUM field, potatoes were planted in the LT_VIE field, and spring wheat was sown in the LT_VEZ field. In these fields, the soil had been ploughed, then cultivated to break up clods and level the surface, and finally prepared for sowing. Therefore, crop residues did not influence the spectral information collected during the UAV and Sentinel-2 acquisitions. In the remaining two fields, soil sampling was carried out after harvest of spring wheat in the LT_LYD and spring barley in the LT_VAL field. Because no-till practices are employed in LT_LYD, crop residues at the sampling date accounted for about 10 − 20% of the soil surface, while in LT_VAL residues constituted less than 10% of the observed surface. The EMI surveys were conducted in late October 2021, the same year as soil sampling and remote sensing data acquisition. An overview of the fields used in the study, including their size, total number and sampling date of ground truth samples, Sentinel-2 data acquisition date, UAV flight and EMI measurement data is provided in Table 1, and a detailed description of the sites is presented below.

2.2.1. *Rumokai test site*

The field at Rumokai (LT_RUM) is located in the south-western part of Lithuania (54°41′51.385″N, 22°59′49.441″E) in the Lower Nemunas limnoglacial plain and covers an area of 2.8 ha. This field belongs to the LAMMC Rumokai experimental station. The topography is uniform and varies between 47 and 48 m above sea level. The average field pH value was 6.3 ± 0.4 (± − standard deviation (SD); range: 5.2 − 7.2), indicating that the soil can be described as slightly acidic. The LT_RUM field falls in the warm and moderately wet agroclimatic zone IIB (Fig. 1). The mean annual temperature is 8.0°C and the annual precipitation is 650 mm. Compared to the other test sites, the predominant soil types are heavy soils, mainly Endocalcaric Gleysols (Siltic, Aric, Drainic, Humic) and Epigleyic Endocalcaric Cambisols (Siltic, Aric, Drainic, Humic) according to the World Reference Base for Soil Resources classification (WRB, 2022). The soils were formed on limnoglacial loam deposits. Crops in the field are grown in 3-course rotation with sugar beet and cereals as main crops, managed conventionally.

Table 1

Summary of the fields used in the study including field name, size, number of soil samples and soil sampling data, UAV flight date, Sentinel-2 data acquisition date, and EMI measurement data.

Field	Area (ha)	Samples (*n*)	Soil sampling	UAV survey	Sentinel-2	EMI survey
LT_RUM	2.8	72 (70)*	2021-05-10	2021-05-10	2021-05-12	2021-10-21
LT_VIE	2.7	70 (66)*	2021-05-10	2021-05-10	2021-05-11	2021-10-20
LT_VEZ	2.3	57(52)*	2021-05-14	2021-05-14	2021-05-12	2021-10-21
LT_LYD	4.7	112 (106)*	2021-08-10	2021-08-10	2021-08-09	2021-10-20
LT_VAL	3.0 (1.7)	77 (39)*	2021-09-10	2021-09-10	2021-09-08	2021-10-19

Note: 77 soil samples were collected in the LT_VAL field but part of the samples covered areas of permanent grassland, so only 39 points from this field were used in this study. During data preparation, several sampling points were removed prior to machine learning because they were located too close to drainage ditches, roads, or trees. Specifically, 6 points were removed from the LT_LYD field, 2 points from LT_RUM, 5 points from LT_VEZ, and 4 points from LT_VIE.

2.2.2. *Vievininkai test site*

The field at Vievininkai (LT_VIE) is located in the eastern part of Lithuania (54°45′17.174″N, 24°46′53.464 E) in the highlands of south-eastern Lithuania and covers an area of 2.7 ha. The landscape in the field is quite hilly and the elevation ranges between 149 and 158 m above sea level. The soil is slightly acidic, with an average pH value of 6.2 ± 0.6 (range: 4.2–7.5). LT_VIE falls in the moderately cool and moderately wet agroclimatic zone IIIB (Fig. 1). The mean annual temperature is 7.2°C, and the annual precipitation is 678 mm. The main soil type is Endocalcaric Luvisols (Loamic) according to the WRB (2022). The field is mainly used for the cultivation of potatoes and cereals under conventional farming practices and belongs to a local farmer.

2.2.3. *Vėžaičiai test site*

The field at Vėžaičiai (LT_VEZ) is located in the western part of Lithuania in the south-western Samogitian undulating moraine plain (55°43′41.118″N and 21°27′36.893″E) and has an area of 2.3 ha. The field belongs to Lithuanian Research Centre for Agriculture and Forestry (LAMMC) Vėžaičiai branch base. The landscape is gently sloping (1 − 3°), with the lowest part towards the South. The average elevation is 59 m above sea level. This site location falls within the moderately cool and wet agroclimatic zone I (Fig. 1). The average annual temperature is 7.7°C, and annual precipitation 910 mm. The soils at the field are Glossic Albic Eutric Retisols (Loamic, Aric, Drainic) and Epigleyic Albic Luvisols (Loamic, Aric), according to the WRB (2022). The average field pH was 4.5 ± 0.4 (range: 4.1–6.4). Therefore, the soil is characterized mostly by very strong acidity. In the field, crops are grown in 3–4 course rotation (mainly spring cereals, peas, etc.) under conventional management.

2.2.4. *Lyduokiai test site*

The field at Lyduokiai (LT_LYD) is located in north-eastern Lithuania, within the Western Aukštaitija upland (55°14′45.139″N, 24°51′13.288″E) and has a size of 4.7 ha. The field is managed by a farmer who has implemented no-till agricultural practices for at least 20 years. The terrain is uniform, with elevations ranging from 109 to 113 m above sea level, and it generally slopes westward at an angle of about 3–5°. The pH levels varied from 5.1 to 7.7, with an average of 5.9 ± 0.7, indicating that the soil has medium acidity. LT_LYD is situated in the cold and moderately wet agro-climatic zone IIIA (Fig. 1). The mean annual temperature is 7.0°C with an annual precipitation of 678 mm. The predominant soil types include Epigleyic Epicalcaric Luvisols (Loamic, Humic), Endogleyic Epicalcaric Luvisols (Loamic, Humic), Eutric Planosols (Loamic, Drainic), and Mollic Eutric Gleysols (Loamic, Drainic, Humic) according to the WRB (2022). In the field, crops are grown in 3–4 course rotation (mainly spring cereals, peas, etc.) under low-input management, and no mineral fertilizers or pesticides are applied.

2.2.5. *Valinava test site*

The field at Valinava (LT_VAL) is located in the central part of Lithuania in the Nevežis morainic plain (55°22′53.916″N, 23°51′47.508″E) and is 3.0 ha in size. Elevation is 61–62 m above sea level. The selected LT_VAL field falls into the moderately cool and dry agro-climatic zone IID (Fig. 1). The mean annual temperature is 7.5°C and the annual precipitation is only 569 mm. The main soil type is Endogleyic Endostagnic Endocalcaric Luvisols (Loamic) according to the WRB (2022), which was formed on the ground moraine loam deposits. The soil is slightly alkaline, with an average pH value of 7.3 ± 0.3 (range: 6.5–7.7). The field belongs to the LAMMC experimental base, and the long-term experiment was established in 1991. At LT_VAL field crops are grown under three levels of management intensity: i) conventional, ii) integrated, and iii) low-organic. The crops include spring barley, red clover, winter wheat, rapeseed, and spring wheat in rotation. Part of the field is perennial grassland, where soil samples were also collected but not used in this study, as bare soil conditions were a prerequisite for the analyses.

2.3. Soil sampling and laboratory analysis

A total number of 388 soil samples were taken from the depth of 0–20 cm from all five fields (Fig. 1). At all locations, the soil was bare at time of sampling. The samples were collected in a regular 20 × 20 m grid, where each sample consisted of three to four sub-samples taken within a 1 m radius. Detailed maps of all points collected are provided in Supplementary Fig. 1. For the chemical and soil textural analysis, the collected soil samples were air-dried and passed through sieves of different sizes in the laboratory (2 mm sieves for textural analyses and 0.25 mm sieves for SOC analyses). SOC content (%) was determined using the Tyurin wet oxidation method, followed by followed by photometric measurement at 590 nm with a UV–VIS spectrophotometer (Cary, Varian) and glucose as the calibration standard. Soil texture was determined by wet sieving and the pipette method according to ISO 11277:2009 (sand fraction = 63 μm to 2 mm). Volumetric soil water content (SWC) of the field fresh soil was determined gravimetrically by the weight loss after oven-drying at 105°C for 24 h, whereby for the volumetric water content undisturbed Kopecky rings of 55 x 35 mm were used. The soil pH was measured potentiometrically employing a 1 M KCl solution in a 1:2.5 (w/v) extract.

2.4. Remote data acquisitions

2.4.1. UAV data acquisition

The UAV system utilized for collecting images of the bare soil surface was the consumer-grade quadrotor Phantom 4 Professional (SZ DJI Technology Co., Shenzhen, China), equipped with a real-time kinematic

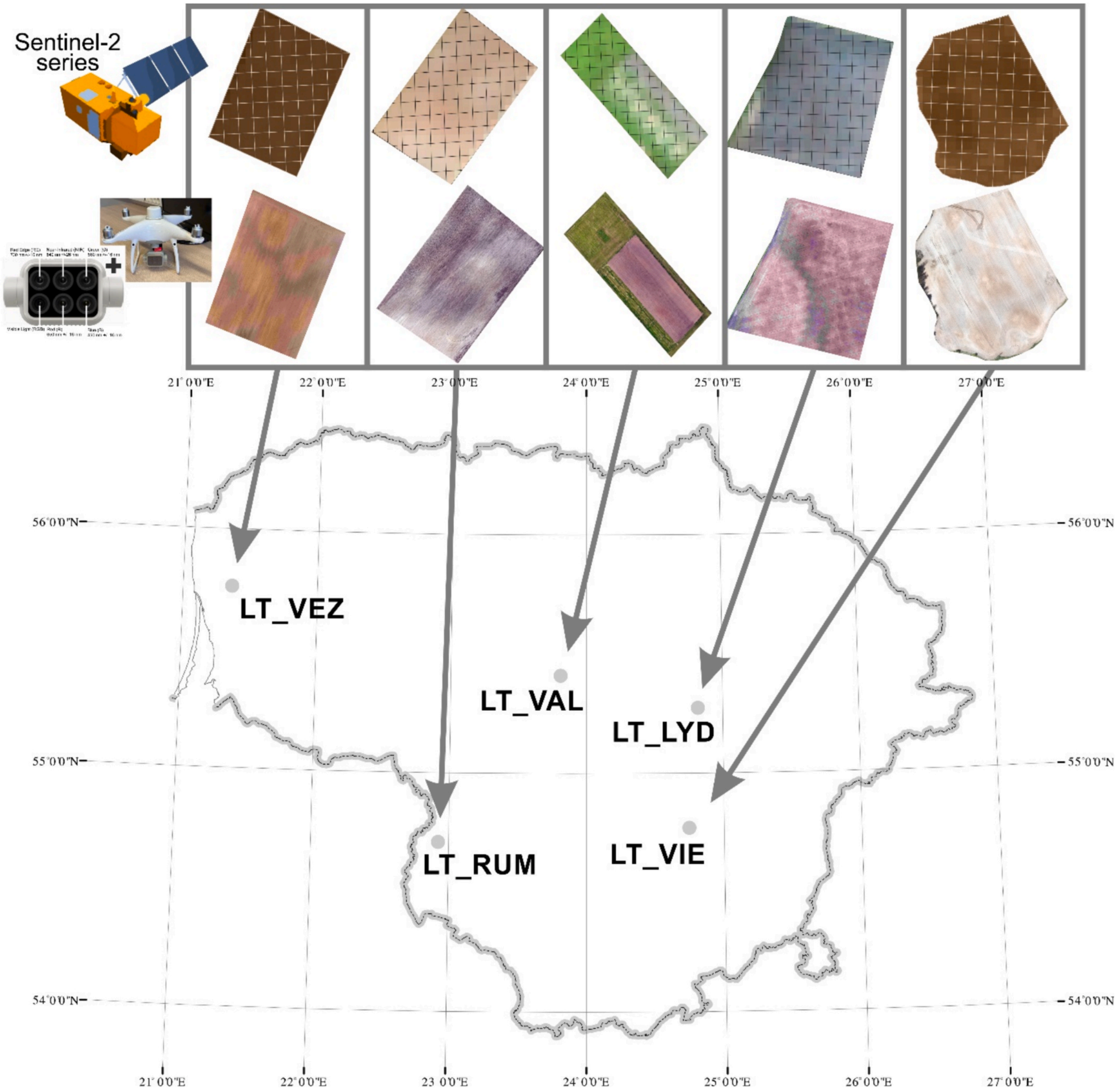

Fig. 2. Colour-composites of Sentinel-2A (top row) and UAV aerial maps (second row) obtained over the bare soil across the five fields located in different pedo-climatic zones in Lithuania.

(RTK) module. The UAV featured an integrated sunlight sensor, which automatically adjusts for radiation reflectance, enabling the direct acquisition of reflectance data. The UAV carried a multispectral imaging system, which included a visible light (RGB) sensor for capturing images in the visible spectrum, and five additional multispectral bands equipped with 5.74 mm focal lenses. These bands encompassed blue light (B), green light (G), red light (R), red edge (RE), and near-infrared (NIR) with central wavelengths at 450, 560, 650, 730, and 840 nm, respectively. All UAV flights were conducted in 2021 on the same day soil samples were collected (Table 1). The Pix4D flight planner app (Pix4D SA, Lausanne, Switzerland) was utilized to design the flight plan, serving as the primary interface between the user and the UAV. In each field, images were captured between 11:00 AM and 1:00 PM local time at a flight altitude of 50 m. All UAV flights took place under clear skies and in conditions of low wind speed. During the flights, the UAV's camera was positioned downward with a course angle of 53°. The total flight duration to cover the entire field lasted approximately 18–25 min (depending on the site), and around 1495–3972 images were captured during each flight with 70% vertical and horizontal overlap.

In this study, the UAV system and camera used are shown in Fig. 2, which also includes the multispectral images of each field surveyed. UAV multispectral image data was pre-processed using the Pix4D software, which employs the structure-from-motion technique. This technique was used to relate features between overlapping images and calculate the 3D position of the matched points, which are densified and textured with the corresponding images. The *ortho*-mosaic image was generated by projecting each texture point onto the 2D plane and was exported in a TIFF image format for further analysis. After the image stitching process, the generated *ortho*-mosaic ground sampling distance was 2.6 cm per pixel.

2.4.2. Sentinel-2 data acquisition

Sentinel-2A multispectral band images (Table 1, Fig. 2) were downloaded from the ESA Sentinel Hub (https://scih****ub.copernicus.eu/) within a maximum interval of two days following ground truth sampling. Images for each band were retrieved individually for the five field sites using pre-designed shape files. In this study, 10 spectral bands were utilized including four bands with a 10 m resolution, namely B2 measured at 490 nm, B3 at 560 nm, B4 at 665 nm, and B8 at 842 nm. Additionally, six bands with a 20 m resolution were selected, namely B5 measured at 705 nm, B6 at 740 nm, B7 at 775 nm, B8A at 865 nm, and two SWIR bands B11 (1.375 nm) and B12 (2.190 nm).

2.5. EMI measurements

Apparent electrical conductivity (EC_a) data were gathered using the DUALEM-21H sensor (Dualem Inc., Milton, ON, Canada) in 2021 (Fig. 3; Table 1). The DUALEM-21H, operating at 9 kHz, is a frequency domain electromagnetic induction (EMI) instrument with a single transmitter (*Tx*) and six receivers (*Rx*) coils, forming an array of horizontal coplanar (HCP) and vertical coplanar (VCP) configurations. The HCP coil separation distances are 0.5, 1, and 2 m, while VCP coil separation distances are 0.6, 1.1, and 2.1 m. The effective depth (ED) and depth of exploration (DOE) represent the depths at which the signal reaches 50 and 70% of the total sensitivity under low induction number approximation for the EC_a measurements and depends only on the *Tx*-*Rx* coil configuration and spacing (S) with 0.9S and 1.6S for HCP, and 0.3S and 0.5S for VCP (Dualem Inc, 2008, Taylor, 2011). In soils with high electrical conductivities (>100 mS m^{-1}), these theoretical depths decrease as the low induction number approximation is compromised (Christiansen et al., 2016).

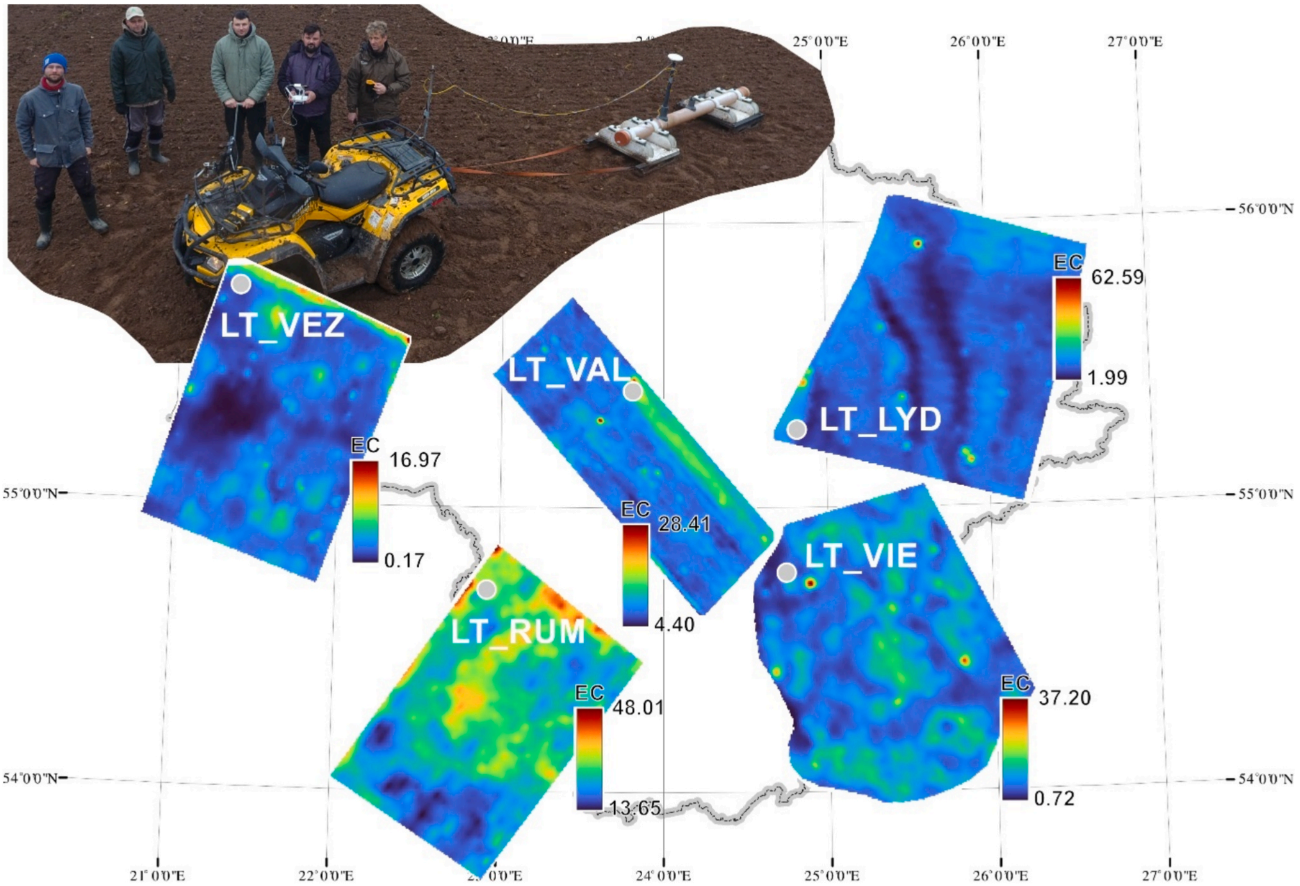

Fig. 3. Maps illustrating the estimated electrical conductivity (EC) mS m^{-1} of the topsoil layer (0 – 20 cm) for the five fields located at different pedoclimatic zones in Lithuania.

The EMI instrument was mounted on a sled at a height of 0.3 m above the ground and was pulled behind an ATV. Sensor measurements were georeferenced using a real-time kinematic (RTK) Global Navigation Satellite System (GNSS) system (Trimble GPS – Trimble Inc, USA). The EMI surveys were conducted in late October the same year as the soil sampling and remote sensing measurements (Table 1). Additionally, on the same day the EMI surveys were conducted, soil samples were collected for SWC measurements. During the EMI surveys, the soil was bare, except for LT_RUM, which had sugar beets planted in rows approximately 55 cm apart, allowing measurements to be conducted without interference. At LT_RUM, the driving line spacing was 5–10 m, with the GPS horizontal positioning being generally accurate to about 5 cm. For LT_LYD and LT_VIE, the driving line spacing was approximately 5 m. However, at LT_LYD, an activation signal for the GPS could not be received, resulting in a horizontal positioning accuracy of less than 50 cm, whereas at LT_VIE the GPS accuracy was around 5 cm. For LT_VAL, the driving line spacing was 3–4 m, and similarly to LT_LYD an activation signal for the GPS could not be received, leading to a horizontal positioning accuracy of just below 50 cm. At LT_VIE field, with a driving line spacing of about 5 m and a successful activation signal for the GPS, the horizontal accuracy of positioning was approximately 5 cm.

The EMI data processing and inversion was performed using the Aarhus Workbench software as described by Auken et al. (2009). Firstly, negative EC_a values were eliminated, and corrections were made for the offset between RTK/GNSS and individual channels. The noise was reduced by manually removing the interference from anthropogenic sources like metal cables, and the signal-to-noise ratio was further improved by averaging data by choosing an appropriate sounding distance and running mean width of 2 and 6 m, respectively. A quasi-three dimensional spatially constrained inversion algorithm using a smoothness constraint (Viezzoli et al., 2008; Auken et al., 2015) was used to estimate the average topsoil electrical conductivity (EC) for a ten-layer subsurface model, with the depth to the top of each layer being 0, 0.2, 0.5, 0.9, 1.4, 2.2, 3.3, 4.8, 7.0, and 10.0 m, respectively, and a uniform initial EC estimate of 25 mS m^{-1}. Afterwards, the retrieved EC point values were interpolated to a 1.6 −m raster using ordinary kriging with an exponential variogram. The variograms were fitted using the *autofitVariogram* function from the R package *automap* (Hiemstra and Skoien, 2025).

2.6. Modelling approach and statistical analysis

The soil properties of each of the five fields were modelled separately, using field-specific soil datasets. This also means that the models established (calibrated) on the training datasets were only tested (validated) on data from the same field. It is important to note that all models were therefore trained and validated within individual fields, reflecting a site-specific modelling approach commonly applied in precision agriculture. Consequently, the reported validation metrics represent within-field predictive performance rather than model transferability across sites.

For each field, the collected soil dataset was split into two subsets with 70% used for training and 30% for validation, using the *createDataPartition* function from *caret* package in R (Kuhn, 2008). To ensure a balanced representation of the target variable in both subsets, stratified sampling was applied. This method preserves the response variable's distribution, reducing potential biases from an even split, especially when certain soil property values are less frequent. By maintaining proportional representation, stratified partitioning improves model generalizability and minimizes the risk of overfitting to specific values ranges. After applying this method, all training and validation subsets were manually reviewed to ensure that the training datasets (used for calibration) encompassed the full range of target variables (soil properties) present in the testing datasets (used for validation) in all simulation scenarios. Remote sensing and proximal datasets were integrated into various modelling scenarios to develop prediction models using the random forest approach. To achieve consistent and spatially comparable data fusion, raster layers from remote sensing and proximal datasets with varying spatial resolutions (Table 2) were standardized through resampling.

Continuous predictor layers were resampled using bilinear interpolation to preserve spatial resolution based on the datasets with the lowest resolution. This ensured spatial consistency and proper integration of all predictors within the modelling framework. Subsequently, the *crop* and *mask* functions from terra package were used to restrict raster extents to the boundaries of the predefined study sites, thereby retaining only relevant spatial information. Furthermore, all raster datasets were projected into a uniform coordinate reference system (EPSG:32635, UTM Zone 35 N). The random forest models were generated in R using the *caret* package (Kuhn, 2008). The seven different modelling scenarios tested, along with additional information such as covariates used and pixel size, are listed in Table 2. These scenarios represent all possible combinations of the three sensor data sources (satellite, UAV, and EMI), reflecting our hypothesis that combining complementary datasets would improve the prediction accuracy of soil properties compared with using individual data sources alone. Overall, 420 simulation runs were performed, encompassing seven modelling scenarios, five fields, and six soil properties for calibration and validation, in order to thoroughly investigate the predictive capabilities of each model.

Table 2
Different modelling scenarios, applied covariates, and spatial resolutions for the prediction of the soil properties.

Number	Scenario	Abbreviation	Covariates	Pixel size
1	Unmanned aerial vehicle	UAV	In total 5: spectral bands (Blue, Green, Red, NIR, Red Edge)	2.6 cm $pixel^{-1}$
2	Electromagnetic Induction	EMI	In total 1: ECa	1.6 m $pixel^{-1}$
3	Sentinel-2a	S2	In total 10: spectral bands (B2, B3, B4, B5, B6, B7, B8, B8A, B11, B12)	10 m or 20 m per $pixel^{-1}$
4	Unmanned aerial vehicle + Electromagnetic Induction	UAV + EMI	In total 6: 5 spectral UAV bands (Blue, Green, Red, NIR, Red Edge) + ECa	1.6 m $pixel^{-1}$
5	Unmanned aerial vehicle + Sentinel-2a	UAV + S2	In total 15: 5 spectral UAV bands (Blue, Green, Red, NIR, Red Edge) + 10 Sentinel-2 spectral bands (B2,B3,B4, B5, B6, B7,B8, B8A, B11, B12)	10 m or 20 per $pixel^{-1}$
6	Electromagnetic Induction + Sentinel-2a	EMI + S2	In total 11: Eca + 10 Sentinel-2 spectral bands (B2,B3,B4, B5, B6, B7,B8, B8A, B11, B12)	10 m or 20 m per $pixel^{-1}$
7	Unmanned aerial vehicle + Electromagnetic Induction + Sentinel-2a	UAV + EMI + S2	In total 16: 5 spectral UAV bands (Blue, Green, Red, NIR, Red Edge) + 10 Sentinel-2 spectral bands (B2,B3,B4, B5, B6, B7,B8, B8A, B11, B12) + ECa	10 m or 20 m per $pixel^{-1}$

2.7. Model prediction accuracy

The prediction capability of the random forest model for both calibration and validation was evaluated by the coefficient of determination (R^2), root mean squared error (RMSE, expressed in %), and the Nash-Sutcliffe Efficiency coefficient (NSE), computed as follows (Wallach, 2006):

$$R^2 = \left(\frac{\sum_{i=1}^{n} (y_i - \overline{y})(x_i - \overline{x})}{\sqrt{\sum_{i=1}^{n} (y_i - \overline{y})^2 \sum_{i=1}^{n} (x_i - \overline{x})^2}} \right) \tag{1}$$

$$RMSE = \sqrt{\frac{1}{n} \sum_{i=1}^{n} (y_i - x_i)^2} \tag{2}$$

$$NSE = 1 - \left[\frac{\sum_{i=1}^{n} (X_i - Y_i)2}{\sum_{i=1}^{n} (X_i - X^{mean})2} \right] \tag{3}$$

where Y_i is the simulated value, X_i is the measured value, n is the number of measurements, and X^{mean} is the arithmetic mean of the measured value X.

R^2 describes the proportion of the variance in measured data explained by the model and ranges from 0 to 1, with higher values indicating less error variance. Lower RMSE values indicate a better fit compared to larger values. NSE values from 0.75 to 1 indicate very good model performance, values from 0.65 to 0.75 indicate good model performance, values from 0.5 to 0.65 indicate satisfactory performance, while values lower than 0.5 indicate only acceptable performance (Moriasi et al., 2007).

To further interpret the RMSE values, the normalized root mean square error (NRMSE) was also calculated.

$$\text{NRMSE} = (\text{RMSE} / \text{mean}\ (\text{observed})) \times 100 \tag{4}$$

The NRMSE values were interpreted using the following classification: less than 10% – excellent prediction, 10–20% – good, 20–30% – acceptable, and greater than 30% – poor. This approach allows for an objective assessment of the relationship between prediction accuracy and analysis costs.

3. Results and discussion

3.1. Field variability of soil properties

As the selected sites had different geological, pedological, and agroclimatic conditions, the samples differed widely in SOC, soil texture, and soil water contents (Fig. 4).

Across all test sites, SOC content ranged from 0.68 to 3.4%. The lowest mean SOC content was found at LT_VIE (1.26%). Slightly higher mean SOC content was observed at LT_VAL (1.5%), and a similar SOC content at LT_LYD (1.64%). The highest mean SOC values were found at LT_VEZ (1.74%) and LT_RUM (1.77%). According to the Lithuanian SOC evaluation scale for mineral soils (Volungevičius et al., 2024), which defines five SOC classes (very low: < 0.58%, low: >0.58–1.16%, moderate: >1.16–1.74%, high: >1.74–2.33%, and very high: >2.33–5.00%), the SOC values from soil samples collected across our five fields fell into all five classes. However, the majority of the samples were within the moderate and high SOC class. Comparing SOC data variability, it was found that the highest variability occurred at the LT_LYD and LT_RUM sites, where the coefficient of variation (CV) was 30 and 24%, respectively. Slightly lower variability was observed at the LT_VIE site (CV 20%), while the least SOC variability was found at the LT_VAL and LT_VEZ sites, with CV values of 14 and 13%, respectively.

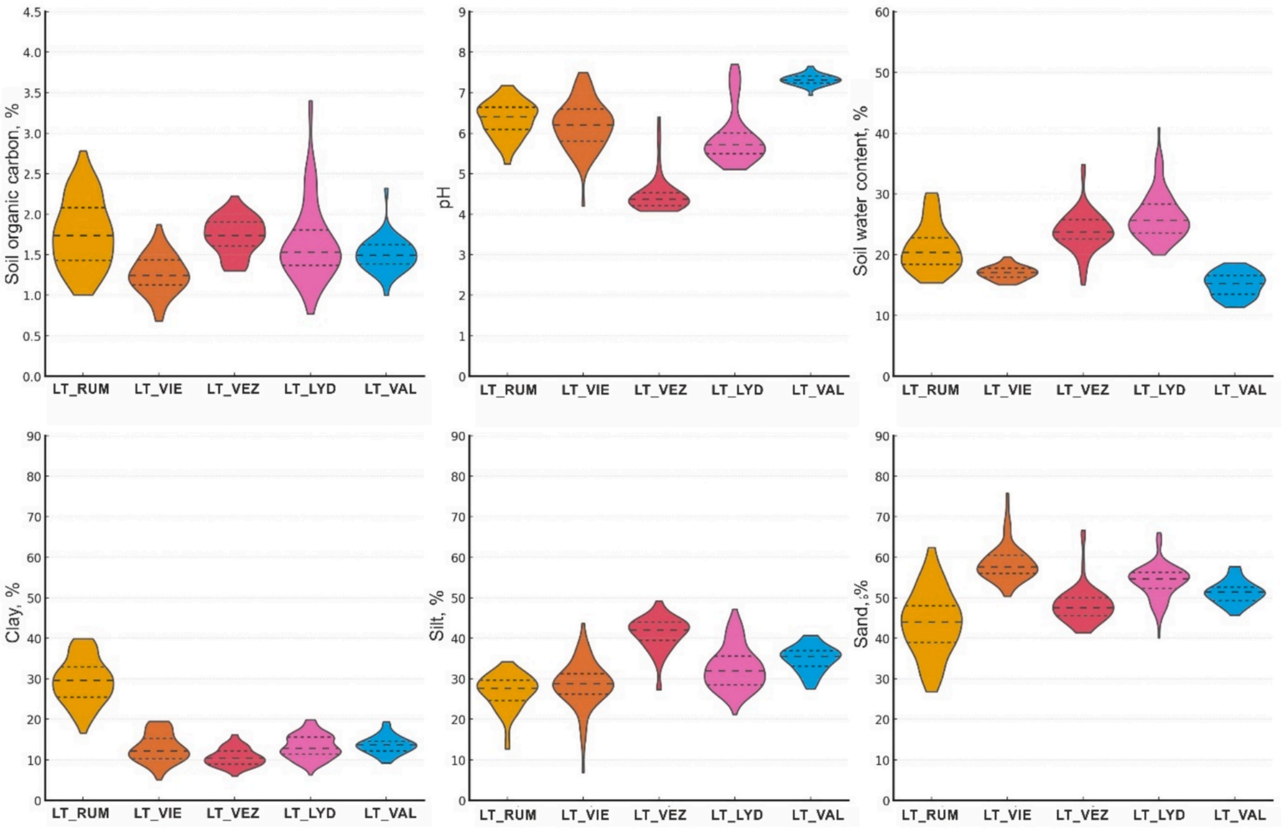

Fig. 4. Violin plots for soil organic carbon (%), pH (–), soil water content (%) (all in upper row) and clay, silt, and sand content (%) in lower row across the five study sites. The central line marks the median value, while the additional horizontal lines represent the first quartile (25th percentile) and the third quartile (75th percentile).

The selected test sites also varied in pH. Across all sites, pH ranged from 4.1 to 7.7. The lowest mean pH was found at LT_VEZ (pH = 4.5, strong acidity). At LT_LYD, the mean pH was 5.9 (medium acidity). The LT_VIE and LT_RUM sites were slightly acidic, with mean pH values of 6.2 and 6.3, respectively. The highest mean pH (7,3) was observed at LT_VAL. At LT_VAL, soils formed on calcareous moraine from the Nemunas glaciation, with carbonates leached and clay illuviation to ~60 cm depth, resulting in a higher pH. pH values within the fields varied only little, with CV ranging from 2% (LT_VAL) to 11% (LT_LYD).

At the time of sampling, the volumetric soil water content (SWC) in the five test sites varied from 11 to 41.0%, representing contrasting soil water conditions both between and within the fields (Fig. 4). The average SWC values varied across the fields, likely due to differences in soil texture and rain events prior to sampling. For example, the highest SWCs were observed in the LT_LYD and LT_VEZ, with average SWCs of 26 and 24%, respectively. These fields experienced rain 2–3 days before sampling. Slightly lower values were found at LT_RUM, where the SWC was 21.2%. The lowest average SWCs were found at LT_VIE and LT_VAL (17.1 and 15.1%, respectively). According to the coefficient of variation (CV), the SWC values varied the most in the LT_RUM site (18.1%) and the least in the LT_VIE site (6.2%).

Soil texture was not uniformly distributed across single fields (Fig. 5). It was dominated by sandy loam and loam for four out of the five fields, except for LT_RUM, which is dominated by clay loam and sandy clay loam.

At LT_VEZ and LT_VAL, a loamy texture dominated, making up 94.7 and 64.1% of the collected samples, respectively, while sandy loam constituted only to 5.3 and 35.9%, respectively. At LT_LYD and LT_VIE, sandy loam dominated at 75.2 and 98.6%, with loam making up 23.9, and only 1.4%, respectively. At LT_LYD, 1% of the samples were sandy clay loam. LT_RUM was the most heterogeneous field with respect to soil texture, as the soil spanned four different textural classes. Clay loam (55.2%) and sandy clay loam (32.8%) were the dominant classes while loam (9%) and sandy loam (3%) constituted minority classes. The studied sites are shaped by fluvioglacial and limnoglacial processes. LT_VAL and LT_RUM, with Cambisols and Luvisols, are fertile with a neutral to slightly alkaline soil reaction, while LT_VIE and LT_LYD, dominated by Retisols, are more sandy and eroded. LT_VEZ, influenced by a wet maritime climate, also has acidic, sandy Retisols.

The correlation matrix (Supplementary Fig. 2) highlights strong site-specific differences in the relationships among soil properties. At LT_RUM, SOC showed moderate correlations with clay ($R^2 = 0.58$), sand ($R^2 = 0.60$) and SWC ($R^2 = 0.59$), indicating coupled physical and chemical controls. In contrast, correlations between SOC and soil texture were considerably weaker at LT_VIE and LT_VAL ($R^2 \leq 0.30$), reflecting more homogeneous or decoupled soil conditions. Across all sites, SWC exhibited generally weak correlations with other soil properties, with LT_RUM being the main exception. Similarly, soil pH consistently showed weak and inconsistent correlations with other soil properties across the fields (R^2 typically 0.01—0.09, with a maximum of ~0.39 at LT_VIE). These weak relationships help explain the generally poor validation performance for pH and SWC compared with SOC and clay.

Heatmaps of squared Pearson correlation coefficients (R^2) among all soil properties (SOC, clay, silt, sand, SWC, and pH) measured at the five sites are provided in Supplementary Fig. 2.

3.2. Model training and validation

3.2.1. Soil organic carbon

In general, the modelled SOC results taken from the best training model for the different data inputs (Table 2) indicated that SOC values were predicted with R^2 values ranging from 0.74 (LT_VAL using EMI data only) to 0.97 (LT_RUM using EMI + Sentinel-2a as inputs) (Supplementary Table 1). Highest R^2 for the validation was found for LT_RUM using Sentinel-2 data only as input ($R^2 = 0.86$) and lowest for LT_VEZ using EMI + Sentinel-2a as inputs ($R^2 = 0.02$) (Table 3). In total, 9% of the validation results exceeded an R^2 of 0.8, 29% an R^2 of 0.6, 49% an R^2 of 0.4, and 34% of all training results R^2 of < 0.2. A total of 11% of the validation results exceeded an RMSE of 0.1%, while 40% had an RMSE above 0.2%. RMSE values greater than 0.4% accounted for only

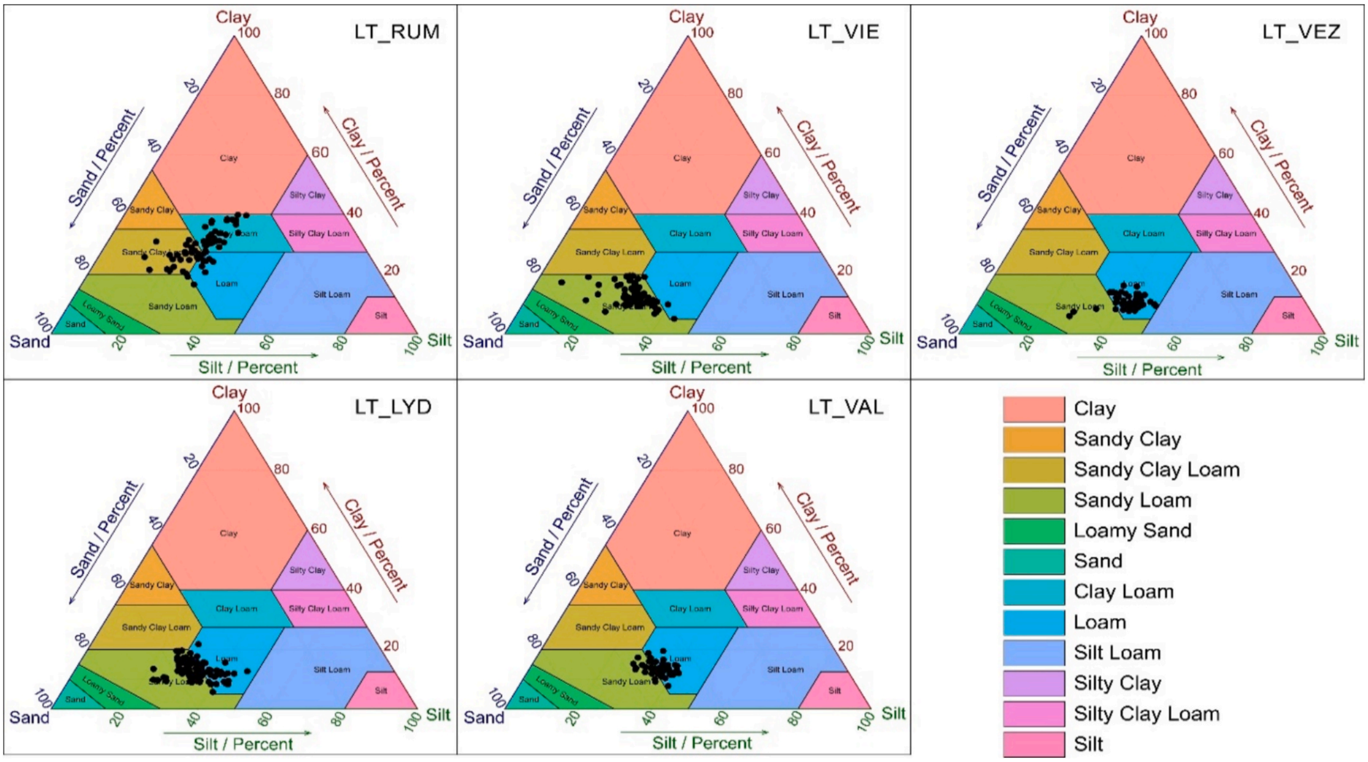

Fig. 5. Soil textural variability for the five fields located in different agroclimatic zones of Lithuania, presented within the USDA textural triangle.

Table 3
Validation (30% of data used) results for predicting soil organic carbon (%), volumetric soil water content (%) and pH using seven different sensor-combination scenarios (Table 2) across the five fields in Lithuania.

Field	Data used (modelling Scenario)	SOC			SWC			pH		
		R^2	RMSE	NSE	R^2	RMSE	NSE	R^2	RMSE	NSE
LT_RUM	UAV	0.84	0.14	0.79	0.73	2.3	0.71	0.06	0.47	0.05
	EMI	0.37	0.35	0.24	0.38	2.89	0.37	0.08	0.4	0.08
	S2	**0.86**	0.15	0.86	0.62	2.8	0.6	0.1	0.39	0.07
	UAV + EMI	0.51	0.29	0.47	0.51	3.04	0.47	0.18	0.38	0.1
	UAV + S2	0.66	0.22	0.63	0.63	2.7	0.62	0.1	0.39	0.29
	EMI + S2	0.61	0.24	0.58	0.66	2.67	0.63	0.15	0.37	0.13
	UAV + EMI + S2	0.67	0.22	0.64	0.63	2.71	0.62	0.08	0.39	0.04
LT_VIE	UAV	**0.41**	0.21	0.26	0.2	1.43	0.16	0.04	0.68	0.09
	EMI	0.19	0.25	0.1	0.02	1.03	0.05	0.18	0.61	0.17
	S2	0.15	0.19	0.13	0.01	1.23	0.01	0.07	0.46	0.08
	UAV + EMI	0.27	0.21	0.24	0.11	0.87	0.02	0.23	0.6	0.22
	UAV + S2	0.25	0.21	0.17	0.01	1.24	0.02	0.12	0.44	0.02
	EMI + S2	0.23	0.18	0.22	0.02	1.22	0.01	0.15	0.43	0.06
	UAV + EMI + S2	0.21	0.21	0.14	0.01	1.23	0.01	0.22	0.4	0.19
LT_VEZ	UAV	0.54	0.15	0.53	0.08	3.74	0.04	0.05	0.28	0.11
	EMI	0.15	0.22	0.07	0.01	3.19	0.09	0.01	0.21	0.03
	S2	0.2	0.27	0.26	0.11	2.89	0.11	0.02	0.45	0.05
	UAV + EMI	0.6	0.14	0.59	0.43	2.75	0.23	0.02	0.2	0.08
	UAV + S2	**0.73**	0.19	0.39	0.19	2.77	0.18	0.02	0.45	0.03
	EMI + S2	0.02	0.28	0.14	0.19	2.83	0.14	0.03	0.41	0.04
	UAV + EMI + S2	0.18	0.22	0.13	0.18	2.79	0.17	0.03	0.41	0.06
LT_LYD	UAV	0.77	0.23	0.74	0.35	3.45	0.35	0.44	0.54	0.42
	EMI	0.1	0.69	0.08	0.01	3.99	0.02	0.1	0.71	0.05
	S2	0.46	0.37	0.34	0.07	3.29	0.03	0.36	0.49	0.32
	UAV + EMI	**0.81**	0.21	0.79	0.21	3.09	0.13	0.28	0.62	0.27
	UAV + S2	0.65	0.32	0.5	0.12	3.27	0.04	0.26	0.52	0.24
	EMI + S2	0.2	0.38	0.16	0.09	3.19	0.08	0.52	0.39	0.47
	UAV + EMI + S2	0.34	0.42	0.19	0.1	3.54	0.07	0.44	0.54	0.42
LT_VAL	UAV	0.19	0.14	0.17	0.16	1.89	0.15	0.03	0.15	0.12
	EMI	0.02	0.14	0.03	0.09	2.05	0.08	0.01	0.12	0.09
	S2	0.45	0.1	0.39	0.15	2.06	0.09	0.04	0.13	0.05
	UAV + EMI	0.02	0.14	0.06	0.12	1.87	0.1	0.31	0.16	0.16
	UAV + S2	0.22	0.12	0.14	0.14	1.98	0.11	0.07	0.14	0.05
	EMI + S2	**0.49**	0.1	0.4	0.14	2.07	0.1	0.04	0.13	0.27
	UAV + EMI + S2	0.42	0.1	0.28	0.13	2.05	0.08	0.01	0.13	0.24

6%. Similar trends were observed in the calculated NSE values. These findings are consistent with other studies. For example, Biney et al. (2023) found that the accuracy of UAV-based SOC prediction models varied depending on the model used, with R^2 values ranging from 0.64 to 0.82, while RMSE ranged between 0.15 and 0.19%. Interestingly, Sentinel-2 outperformed UAV at the LT_VAL and LT_VIE sites, and equaled UAV at the LT_RUM site, presumably due its SWIR bands which match the clay features (Gomez et al., 2022) all the more than for LT_RUM and LT_VIE, SOC and clay are correlated (Supplementary Fig. 2). Additionally, the LT_VAL site is relatively homogeneous, with low SOC variability (Fig. 4) and a smooth soil surface, where high-resolution UAV imagery mainly captures micro-scale surface noise rather than meaningful SOC patterns. Consequently, the coarser Sentinel-2 pixels average out this noise and better represent field-scale SOC variability, resulting in more robust predictions. Summarizing all study sites and the modelling scenarios used, the order of fields based on better SOC prediction results can be ranked as follows: LT_RUM > LT_LYD > LT_VEZ > LT_VIE > LT_VAL. This field ranking based on validation accuracy differs somewhat from earlier studies that used the same data. For instance, Castaldi et al. (2023), which utilized results from three sites and Sentinel-2 data alone, ranked fields as LT_RUM > LT_VAL > LT_VEZ. However, that study applied four pixelwise temporal mosaicking methods that compared Sentinel-2 time series under pure bare soil conditions, driest soil conditions, average bare soil conditions, and dry conditions excluding extreme reflectance values. Additionally, different machine learning models were used, resulting in R^2 values for LT_RUM ranging from 0.42 to 0.94 (average 0.71), for LT_VAL from 0.01 to 0.87 (average 0.43), and for LT_VEZ from 0.01 to 0.26 (average 0.07). Similarly, somewhat different results were obtained in another study by Wetterlind et al. (2025). Using Sentinel-2 data and RF models, fields ranked according to SOC prediction accuracy as follows: LT_VEZ > LT_LYD > LT_VAL > LT_VIE. This variation emphasizes that both the spectral image acquisition methods, the data incorporated (series vs single date) and their processing approaches greatly impact the prediction accuracy.

These results align with a previous study, where it was observed that satellite-based models across various scales tend to perform best in sites with a wider range of measured SOC content (Vaudour et al., 2022). The two fields with the highest model performance accuracy (LT_RUM and LT_LYD) also exhibited the greatest SOC variation (see Fig. 4) compared to the other sites.

Analysing individual scenarios, specifically the first three scenarios (Table 2, Scenarios 1–3) where only individual sensors were used, it was observed that the best results were in general achieved using UAV or Sentinel-2 data, while EMI alone did not show good results for predicting SOC values at all. The reason why EMI fails to predict SOC can be seen in the physical quantity the sensor measures, as EC_a is a composite of different soil properties such as soil water content, soil pore electrical conductivity, and soil particle surface charge which are all impacted by various soil properties such as soil texture, water retention characteristics, SOC content, fertilization practices, and bulk density (e.g., Kaufmann et al., 2019; Schmäck et al., 2021). Notably, at LT_VAL Sentinel-2 clearly outperformed UAV, possibly due to broader spatial representation from the satellite data, reducing the influence of small-scale variability that can affect UAV imagery. UAV data calibration involved averaging several pixels around sample points, potentially introducing uncertainties related to spatial heterogeneity.

Moreover, combining different sensor data (Table 2, Scenarios 4–7), often yielded varied results. For example, combining UAV data with other sensor data often resulted in decreased SOC prediction accuracy, likely due to resolution discrepancies. In contrast, combining EMI datasets with other sensor data often slightly improved the SOC prediction. Similar findings have been reported in other studies. For example, Mahmood et al. (2012) demonstrated that combining an NIR spectrometer with a handheld EMI sensor (EM38) can improve the prediction accuracy of soil properties (e.g., SOC, soil texture) compared to using each sensor individually. Similarly, Wetterlind et al. (2015) found that the Vis-NIR spectrometer was the best individual sensor for predicting soil properties (such as SOM and soil texture). However, EC_a data provided additional information and, in many cases, yielded predictions that were equally good or even better than those obtained with the Vis-NIR sensor.

3.2.2. Volumetric soil water content

Overall, the simulation results based on random forest model showed relatively high R^2 and NSE values, with low RMSE for the training data set (Supplementary Table 1). However, during the validation stage, the statistical metrics significantly deteriorated, with the model performing adequately in predicting SWCs only in the LT_RUM field mostly exceeding R^2 values of 0.6, with the exception of the use of EMI data only, with an R^2 of 0.38 (Table 3). For all other fields, the R^2 values never exceeded 0.2 with the exception for LT_VEZ with an R^2 of 0.42, LT_LYD with R^2 of 0.35 (UAV) and 0.21 (UAV + EMI), and LT_VIE with an R^2 of 0.20 (UAV). During the validation phase, RMSE values ranged from 0.9% to 4.0%, while NSE values varied from 0.01 to 0.71. The LT_RUM field was characterized by a higher clay content and larger textural variability compared to the other fields (Figs. 4 and 5), However this did not lead to larger variation in SWC measures compared with the other fields, except for LT_VIE and LT_VAL, and therefore, SWC variability seems not to be the main reason for the better models at LT_RUM. Nonetheless, LT_RUM showed the strongest correlations between measured SWC and soil texture among all fields, with R^2 values of 0.50 for sand, 0.44 for clay, and 0.22 for silt (Supplementary Fig. 2), suggesting that spatial patterns in SWC may have been more strongly governed by underlying textural variation. Evaluating the first three modelling scenarios for the LT_RUM field, the best results were observed when using UAV and Sentinel-2 data, while the results were poorer when using EMI data only. The reason for the poor performance when EMI data are used have been already discussed for the SOC prediction. Analysing the remaining four modelling scenarios (Scenario 4–7) for the same field, it can be concluded that regardless of the sensor combinations used, the SWC modelling results were very similar. As mentioned, for the remaining four fields, the validation yielded low predictive power, and it is difficult to conclude which sensor might be best suited for the prediction. This may be partly attributed to varying soil water contents across the fields. The LT_LYD and LT_VEZ fields experienced rainfall $2-3$ days before sampling, leading to the highest measured SWCs in these fields. However, as shown by Chen et al. (2025), SWC predictions tend to be less precise during the rainy season compared to dry periods, highlighting the challenges predicting SWC under changing weather conditions. After rainfall, even sandy soils with low organic carbon may temporarily hold high water content, reducing variability driven by soil properties and thus making modeling more difficult. When comparing sensors and their combinations, it is important to consider that EMI measures EC_a over larger depth, and in our case the shallowest depth increment was 0–20 cm, even after the raw data had been inverted. In contrast, Sentinel-2 and UAV sensors detect only the very top of the soil surface, typically millimeters to a few centimeters deep (Babaeian et al., 2019). Studies attempting to correlate surface reflectance with deeper soil water contents found that accuracy decreases substantially with increasing depth (Hegazi et al., 2023). Clearly, these differences in sensing depth directly affect the accuracy and reliability of SWC models.

3.2.3. pH

Overall, the simulation results using the random forest model demonstrated relatively high R^2 and NSE values, along with low RMSE for the training dataset (Supplementary Table 1). However, the statistical performance declined notably during the validation phase (Table 3). During the validation phase, R^2 values decreased, with a maximum of 0.52 observed for LT_LYD (EMI + Sentinel-2). During the validation phase, RMSE values ranged from 0.10 to 0.70, while NSE values varied between 0.02 and 0.47. The poor validation performance is mainly explained by limitations of the predictor variables rather than by the modelling approach. Soil pH does not exhibit a strong or direct response in soil spectral reflectance (Stenberg et al., 2010) or apparent electrical conductivity at the field scale, except where carbonates occur in shallow soil layers. In this study, carbonates were absent in LT_VEZ, occurred in the upper soil layers at LT_LYD due to soil erosion, and were located at depths of approximately 40–150 cm in the remaining fields, largely below the sensing depth of the applied sensors. In addition, the relatively narrow within-field pH variability at most sites constrained the ability of the random forest models to learn robust predictive relationships. Slightly better yet insufficient results were obtained for LT_LYD, likely due to the combination of the highest within-field pH variability among the study sites (Fig. 4) and the presence of carbonates in the upper soil layers caused by soil erosion. In the remaining four fields, pH predictions were consistently poor across all modelling scenarios, reflecting the non-linear and indirect relationships between pH and environmental variables, as well as the absence of a direct influence of pH on apparent electrical conductivity or vis–NIR spectral reflectance.

In contrast to our pH prediction results, Gogumalla et al. (2022) found that satellite-based predictions were able to estimate pH values during the validation phase with a relatively high correlation coefficient (R^2) of 0.32 and an RMSE of 0.78. However, it is important to note that their model training and validation were based on 2,244 soil samples, which is 95–98% more data than those used in our study. In other studies, with smaller sample sizes, pH prediction results using random forest model during the validation phase were also poor. For example, a study by Bouslihim et al. (2024), who used 191 soil samples, reported an R^2 of only 0.26 and an RMSE of 0.15 for the pH prediction. While the number of samples may play a role, the broader geographical extent is also likely an important factor. Larger areas tend to encompass greater variability in parent material, soil properties, and land use, which may help improve model performance compared to field-scale studies.

3.2.4. Clay

Analysing the outcomes across all fields and the seven modelling scenarios for clay prediction, it was observed that the R^2 values were relative high during the training phase (Supplementary Table 2). However, during the validation phase, these values significantly decreased from 0.01 and to highest R^2 with 0.79 calculated for LT_VEZ (UAV + EMI) (Table 4). During the validation phase, RMSE values ranged from 1.26 to 4.29%, while NSE values varied between 0.03 and 0.59, reflecting a notable decrease in prediction accuracy compared to the training phase. Most experiments analysing topsoil clay predictions have yielded similar results. For example, a synthesis of 70 reviewed articles found that, when using satellite-based RF models to predict clay particle content, R^2 ranged from approximately 0.1 to 0.80, while RMSE values

Table 4
Validation (30% of data used) results for the prediction for clay, silt and sand fraction (%) using seven sensor combination scenarios (Table 2) across five fields in Lithuania.

Field	Data used (modelling Scenario)	Clay			Silt			Sand		
		R^2	RMSE	NSE	R^2	RMSE	NSE	R^2	RMSE	NSE
LT_RUM	UAV	0.53	4.09	0.47	0.05	4.91	0.02	0.51	6.01	0.45
	EMI	0.54	4.29	0.47	0.03	4.01	0.03	0.32	5.93	0.27
	S2	0.64	3.95	0.58	0.35	2.99	0.26	0.51	5.52	0.51
	UAV + EMI	0.59	3.81	0.51	0.04	4.78	0.02	0.44	6.21	0.42
	UAV + S2	0.55	4.24	0.52	0.28	3.27	0.11	0.47	5.75	0.46
	EMI + S2	0.59	3.65	0.58	0.34	2.94	0.29	0.49	5.65	0.48
	UAV + EMI + S2	0.58	4.06	0.56	0.34	3.09	0.21	0.46	5.75	0.46
LT_VIE	UAV	0.45	3.17	0.43	0.1	5.33	0.16	0.02	3.99	0.03
	EMI	0.57	2.19	0.56	0.01	6.11	0.05	0.02	7.13	0.02
	S2	0.41	3.21	0.34	0.06	5.79	0.06	0.02	3.54	0.06
	UAV + EMI	0.45	2.7	0.44	0.02	5.55	0.02	0.16	6.05	0.06
	UAV + S2	0.56	3.1	0.29	0.05	5.24	0.05	0.08	3.34	0.03
	EMI + S2	0.43	3.24	0.49	0.12	6.49	0.06	0.05	3.76	0.05
	UAV + EMI + S2	0.54	3.04	0.46	0.12	5.79	0.16	0.06	3.47	0.03
LT_VEZ	UAV	0.48	1.83	0.45	0.15	3.47	0.13	0.23	2.52	0.11
	EMI	0.66	1.5	0.59	0.42	3.97	0.41	0.46	2.21	0.43
	S2	0.3	2.6	0.31	0.11	2.84	0.09	0.07	2.43	0.04
	UAV + EMI	0.79	1.26	0.71	0.54	3.71	0.49	0.46	3.14	0.45
	UAV + S2	0.37	2.02	0.31	0.4	2.44	0.33	0.08	2.58	0.17
	EMI + S2	0.45	1.82	0.46	0.18	2.86	0.12	0.06	2.44	0.05
	UAV + EMI + S2	0.46	1.85	0.34	0.31	2.63	0.23	0.05	2.65	0.03
LT_LYD	UAV	0.36	2.41	0.32	0.47	4.17	0.43	0.37	3.47	0.34
	EMI	0.34	3.04	0.34	0.12	5.57	0.12	0.03	5.14	0.04
	S2	0.46	2.37	0.41	0.43	3.76	0.41	0.11	3.45	0.06
	UAV + EMI	0.42	2.39	0.41	0.55	3.97	0.49	0.43	3.46	0.37
	UAV + S2	0.56	2.29	0.45	0.49	3.61	0.45	0.23	3.16	0.22
	EMI + S2	0.38	2.31	0.37	0.4	4.09	0.35	0.14	4.08	0.14
	UAV + EMI + S2	0.43	2.41	0.4	0.5	4.19	0.43	0.15	3.89	0.14
LT_VAL	UAV	0.19	2.67	0.39	0.01	3.58	0.08	0.12	3	0.27
	EMI	0.1	2.15	0.14	0.02	3.84	0.03	0.21	2.95	0.12
	S2	0.01	1.9	0.03	0.08	3.74	0.17	0.11	3.01	0.09
	UAV + EMI	0.17	1.79	0.15	0.17	3.22	0.13	0.57	2.73	0.45
	UAV + S2	0.02	1.82	0.04	0.02	3.64	0.11	0.06	3.15	0.01
	EMI + S2	0.13	1.84	0.17	0.02	3.7	0.15	0.1	3.06	0.06
	UAV + EMI + S2	0.11	1.8	0.12	0.03	3.58	0.07	0.04	3.21	0.04

varied between 0.5% and 10% (Mgohele et al., 2024).

When comparing sites, the models achieved the highest clay-prediction accuracy at LT_RUM (R^2 – 0.53–0.64, RMSE – 3.65–4.29), followed by LT_VIE, LT_VEZ, and LT_LYD, with the lowest accuracy at LT_VAL (R^2 – 0.01–0.19, RMSE – 1.79–2.67). Notably, the LT_RUM field differed from the other four fields by the fact that the clay content was approximately twice as high as in the other fields (Fig. 4). Additionally, it was dominated by two textural classes: clay loam and sandy clay loam (Fig. 5). These factors likely contributed to better modelling results. Gomez et al. (2022) found that shortly after rain events, the accuracy of clay estimation drastically decreases, confirming the importance of selecting dry soil conditions for the data acquisition. However, excessively dry soils are also likely to result in a similar reduction in prediction accuracy as overly wet conditions. Therefore, optimal moisture levels should be targeted for data collection. These observations align with our results, as LT_LYD and LT_VEZ experienced rain 2–3 days before sampling and data acquisition, which likely degraded the modelling outcomes.

The strong performance of EMI for clay prediction reflects the close relationship between apparent ECa and soil texture. At the field scale, apparent ECa showed a moderate to strong correlation with clay content ($R^2 = 0.39–0.50$). Analysing individual scenarios, specifically the first three scenarios (Table 2, Scenarios 1–3), where only individual sensors were used, EMI data inclusion resulted in the most accurate predictions for LT_VEZ and LT_VIE, while Sentinel-2 data provided the best clay content predictions for LT_RUM and LT_LYD. Examining the sensor contributions (Scenarios 4–7), one can also see that combining multiple sensors did not consistently improve the accuracy. In contrast, the relationship between apparent ECa and SOC was considerably weaker ($R^2 \leq 0.25$), explaining why EMI performed well for clay but poorly for SOC (see 3.2.1.).

3.2.5. *Silt*

Analysing the results for the silt fraction, a similar trend was observed, with statistical metrics showing better performance during the training phase compared to the validation phase (Supplementary Table 2). During the validation phase, the maximum R^2 observed was 0.55 (LT_LYD UAV + EMI) (Table 4). RMSE values ranged from 2.44 to 6.55%, and NSE values also indicated reduced model performance.

Despite the poor performance of the silt predictions, they are consistent with findings from other studies. For example, a review by Mgohele et al. (2024) indicated, that silt predictions vary widely, with R^2 values ranging from approximately 0.16 to 0.75 and RMSE values from 1% to 14%. When comparing the silt predictions to those of clay, the results were considerably worse. Only two fields – LT_LYD and LT_VEZ – demonstrated acceptable prediction performance in most scenarios. In the LT_RUM field, acceptable results were achieved only by adding Sentinel-2 data, while in LT_VIE and LT_VAL none of the sensors or combinations yielded any good predictions.

3.2.6. Sand

The results for sand fraction prediction showed high R^2 values during the training phase (Supplementary Table 2), but these values notably decreased during the validation phase (Table 4).

During the validation phase, R^2 values ranged from 0.02 to 0.57 (LT_VAL UAV + EMI), RMSE varied widely between 2.21 and 7.13%, and NSE values ranged from 0.01 to 0.51, indicating considerable variability in prediction accuracy.

Again, the review by Mgohele et al. (2024) highlighted that sand predictions using remote sensing data exhibit considerable variability, with R^2 values ranging from approximately 0.24 to 0.78 and RMSE values from 1 to 18%.Comparing all fields and the various modelling scenarios, it can be concluded that the highest accuracy for sand prediction was achieved only in the LT_RUM field. This field exhibited the greatest variability in sand contents, ranging from 26.8 to 62.4%, compared to the other four study sites (Fig. 4), pointing to the fact that a certain variability in the predictor is needed for robust prediction.

3.3. Variable importance in projection (VIP) analysis

To identify the most important sensors or sensor combinations defined in the scenarios listed in Table 2, a Variable Importance in Projection (VIP) analysis was performed, which provides valuable insights into the contribution of different covariates for predicting the soil properties (Fig. 4). The VIP analysis was performed only for soil properties where the prediction accuracy was relatively high and reliable, holding in our case for SOC and clay contents. The average VIP score among the five sites and seven modelling scenarios for each band and its standard error are shown in Figs. 6 and 7.

The analysis of VIP scores for the SOC prediction highlights the significant value of integrating data from multiple sensors to improve SOC prediction accuracy as shown in Fig. 6.

The findings of the VIP for each scenario shows that for the UAV-only scenario the red band was identified as the most important variable followed by the NIR band but the green and blue band also contributed to the same extend as the NIR to the prediction. For the Sentinel-2 scenario B8 and B8A were the most influential covariates, while B11, B4, and B2 bands also contributing but to a lesser extent. According to Gholizadeh et al. (2018), the strongest relationships between SOC and Sentinel-2 bands were observed in B4 and B5, followed by B11 and B12. Similar variable importance results for SOC prediction were obtained by Castaldi et al. (2023), where, depending on the model used, B12 and B11 (both SWIR) had the highest importance, followed by B2 (blue) and B4 (red). Combining UAV and EMI data (UAV + EMI scenario), the UAV red band remained the main covariate, followed by EC data measured by EMI. In the combination of UAV and Sentinel-2 data (UAV + Sentinel-2), the red band remained as the most important covariate followed by B8A (vegetation red edge) and B6 (vegetation red edge) bands. Also, the Red Edge bands from UAV, B8 (NIR), and B4 (red), highly contributed to the prediction. In case of the sensor combination EMI + Sentinel-2 (EMI + Sentinel-2), EC data had the greatest impact on SOC predictions, followed by B11 and B8, whereby B4 and B3 also show an important contribution. Finally, for the UAV + EMI + Sentinel-2 combination again the importance of EC data is highlighted, followed by the UAV Red band, and Sentinel-2 bands B8, B11, B12, and B4.

For the clay prediction the UAV data integration showed most impact from Red and NIR bands, while the green band was the least important one (Fig. 7). This pattern is consistent with soil spectral theory, as clay minerals primarily influence soil reflectance through their effects on soil moisture dynamics and surface roughness, which are strongly captured

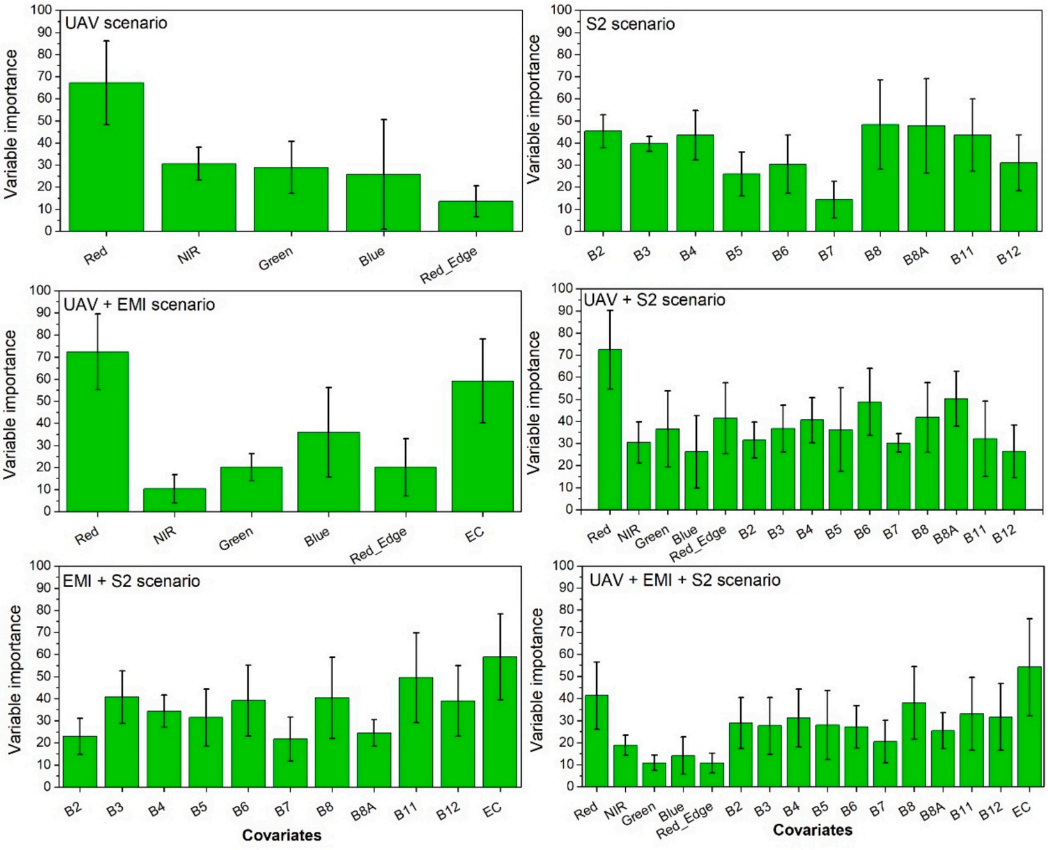

Fig. 6. Average Variable of Importance in Projection (VIP) scores for the soil organic carbon (SOC) prediction models across six modelling scenarios, along with their standard errors (depicted in black), among the five study sites in Lithuania.

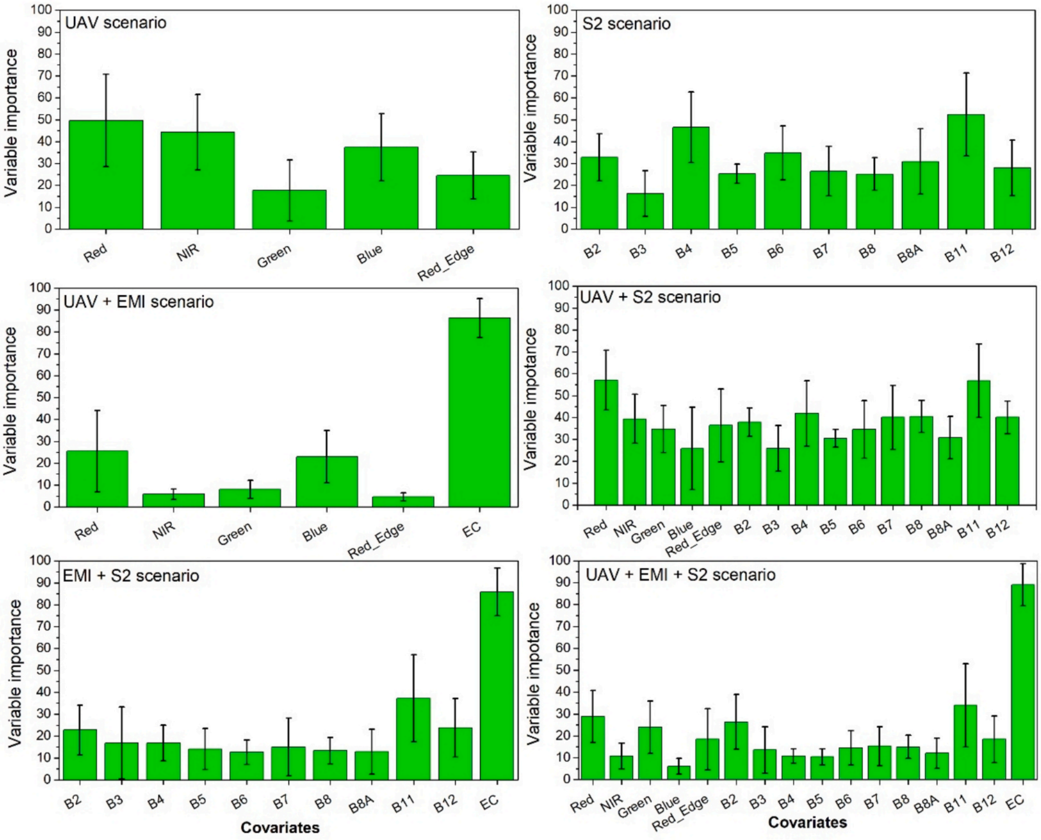

Fig. 7. Bar plots illustrating the average Variable of Importance in Projection scores for the clay particle prediction model across six modelling scenarios, along with their standard errors (depicted in black), among the five study sites in Lithuania.

in the NIR and SWIR regions, whereas visible bands are generally less sensitive to clay content.

Similar results were obtained by Mgohele et al. (2024), who demonstrated that the NIR band contributes the most to predicting clay contents. It is well known that the NIR band is particularly sensitive to SWC and soil organic carbon, which are closely associated with clay minerals. In the Sentinel-2 case, the most important covariates were B11 and B4, whereby the remaining Sentinel-2 bands had quite similar importance, except for B3, which was the least important one. Other authors obtained slightly different results. For example, Gholizadeh et al. (2018) showed that for clay, which was successfully predicted using Sentinel-2 data in a Luvisol, the most important Sentinel-2 band was B7. Wetterlind et al. (2025), found B4 and B6 to be more important in Sentinel-2 models predicting SOC compared with models predicting clay content, whereas B12 were more important for clay models, in a study including 17 sites across Europe. In Scenario 3 (UAV + EMI), EC data showed again a large contribution to the prediction, while the red and blue bands were much less influential. If UAV and Sentinel-2 data were combined (Scenario 4), the three most important covariates were the red band, B8A, and B6 bands, followed by the Red Edge bands from UAV and B8 (NIR). All other remaining bands had quite similar levels of importance for the prediction. Scenario 5 where EMI and Sentinel-2 data were used, EC data was again the most important covariate, while the SWIR bands B11 and B12 were considerably less important than EC. Lastly, in the scenario where all data have been used (UAV + EMI + Sentinel-2), EC data remained the most important covariate, followed by B11, the Red band from UAV, and Green band from UAV as well as B2 (Blue) band from Sentinel-2.

3.4. SOC and clay mapping

We collected a dataset with highly detailed spatial information on soil properties at the field scale. Field data, combined with remote and proximal sensing variables, were used to develop RF models. Based on this model's predictions, we generated SOC (Figs. 8 and 9) and clay content maps (Figs. 10 and 11) at different resolutions (2.6 cm pixel^{-1}, 1.6 m pixel^{-1}, and 10 m pixel^{-1}; see Table 2). As shown, the SOC and clay predictions showed best performance and were therefore selected for mapping (see Section 3.2).

The topography of the LT_RUM field is mostly uniform, resembling a near-level surface, which results in a low erosion risk. However, as shown in Fig. 8, the field can be divided into at least two distinct zones. In the western part of the field, the highest SOC values were measured with the majority of pixels exceeding 2%, whereas in the eastern part SOC values were the lowest and only slightly above 1%.

In general, regardless of the modelling scenario used, all approaches were able to visually distinguish these two SOC zones. Despite differences in resolution among the modelling scenarios, the spatial pattern of SOC remained largely consistent. The only exception was the scenario using EMI data only, where some irregular patterns were observed that did not align with the other scenario derived maps. This discrepancy is also evident in Table 3, where according to statistical measures, the EMI-only scenario yielded the least accurate results compared to the others.

The topography of the LT_LYD field is also relatively uniform with slight variations in elevation (Fig. 9). The terrain generally slopes westward at a gentle angle. The field is characterized as a broadly undulating plateau and is highly susceptible to erosion. As a result, SOC distribution is primarily influenced by soil erosion processes. Due to this, along with increased soil water retention in lower slope positions, the highest SOC values were measured in the central lower parts of the

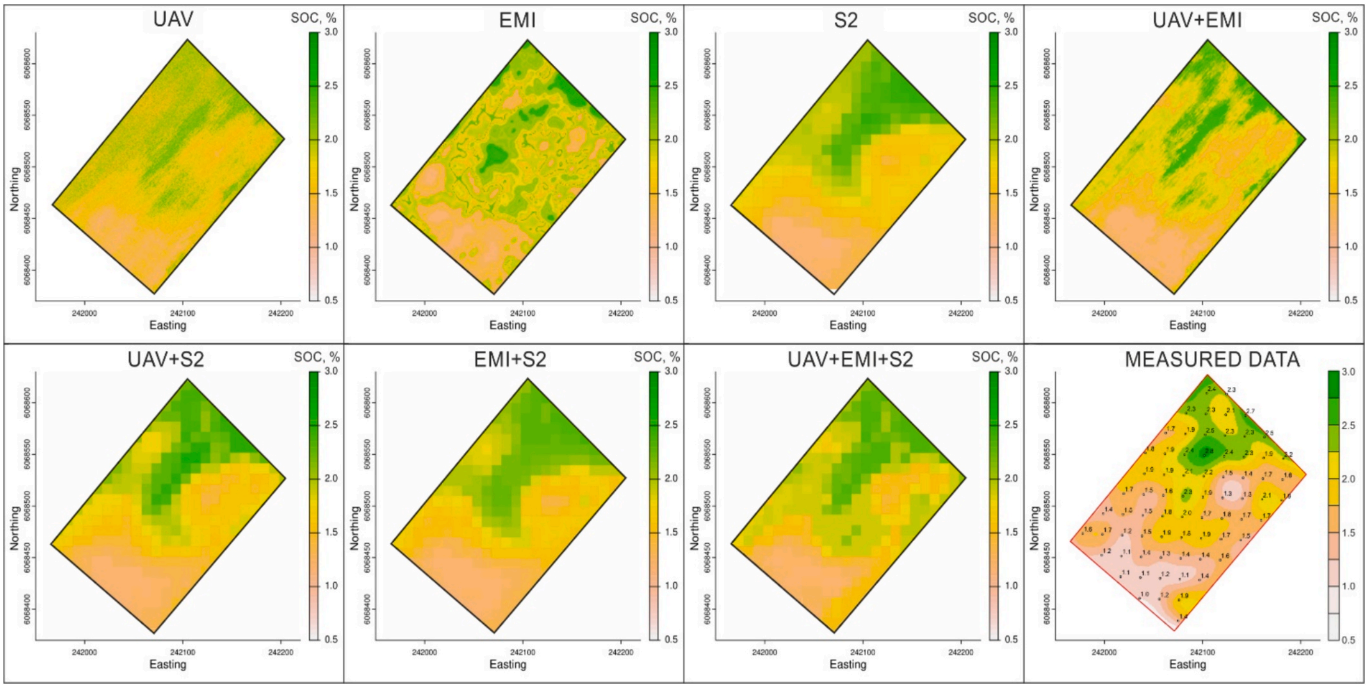

Fig. 8. Soil organic carbon (SOC) maps for the LT_RUM field and all modelling scenarios, along with the interpolated measured data (bottom right). The axes represent coordinates in the Universal Transverse Mercator (UTM) system.

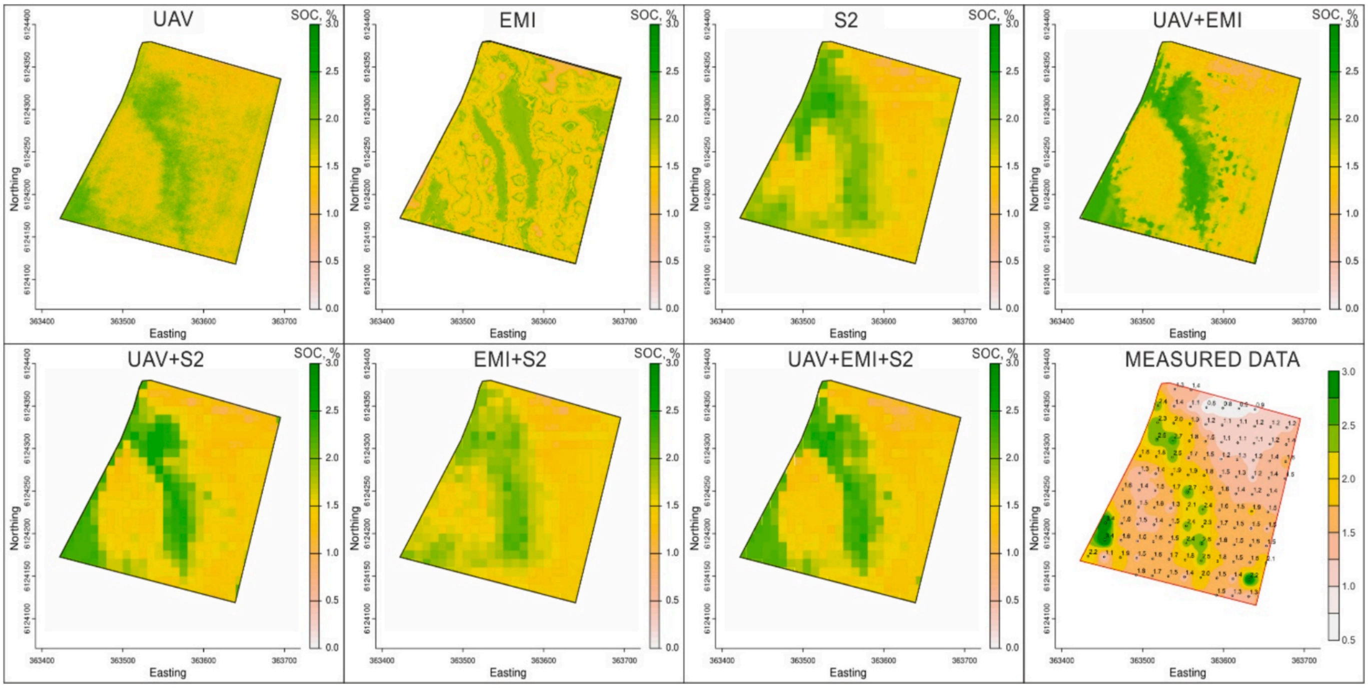

Fig. 9. Soil organic carbon (SOC) maps for the LT_LYD field and all modelling scenarios, along with the interpolated measured data (bottom right). The axes represent coordinates in the Universal Transverse Mercator (UTM) system.

slope, where SOC concentrations often exceeded 2.3%. In contrast, the lowest SOC values were observed in the western part of the field, ranging approximately between 0.8% and 1.2%. As seen in Fig. 9, the majority of modelling scenarios successfully captured the field variations, which were primarily influenced by the slope. However, similar to the LT_RUM field, when using only EMI data or EMI in combination with other sensors (EMI + Sentinel-2; UAV + EMI + Sentinel-2), some unusual patterns were observed. This suggests that EMI datasets often perform worse than UAV or Sentinel-2 data when predicting SOC levels.

For clay mapping in the LT_RUM field, a very similar pattern to that of SOC mapping (Fig. 10) was observed. This is likely due to the similar spatial distribution and therefore correlation of SOC and clay, as confirmed by the R^2 value of 0.58. The prediction results for clay using the seven different modelling scenarios were highly consistent with R^2 values ranging between 0.53 and 0.60, and RMSE values between 3.7 and 4.3 (see Table 4). Visually, differences in clay mapping were more

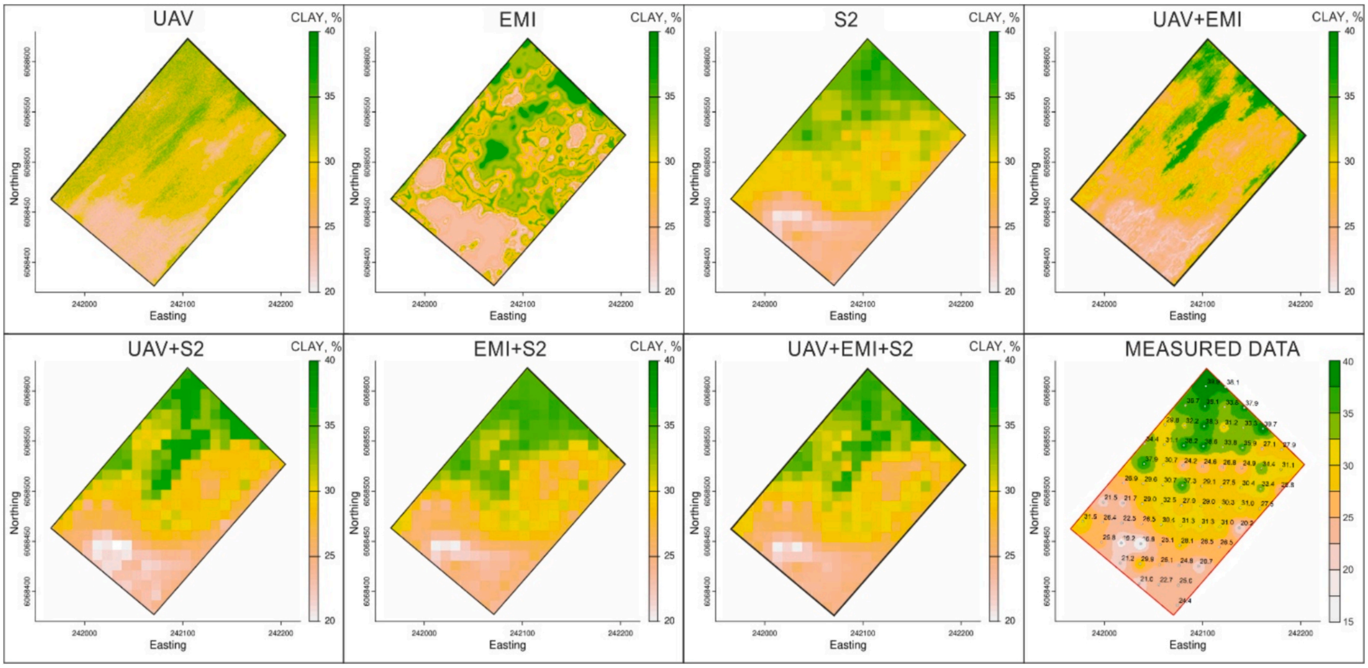

Fig. 10. Clay particle maps for the LT_RUM field and all modelling scenarios, along with the interpolated measured data (bottom right). The axes represent coordinates in the Universal Transverse Mercator (UTM) system.

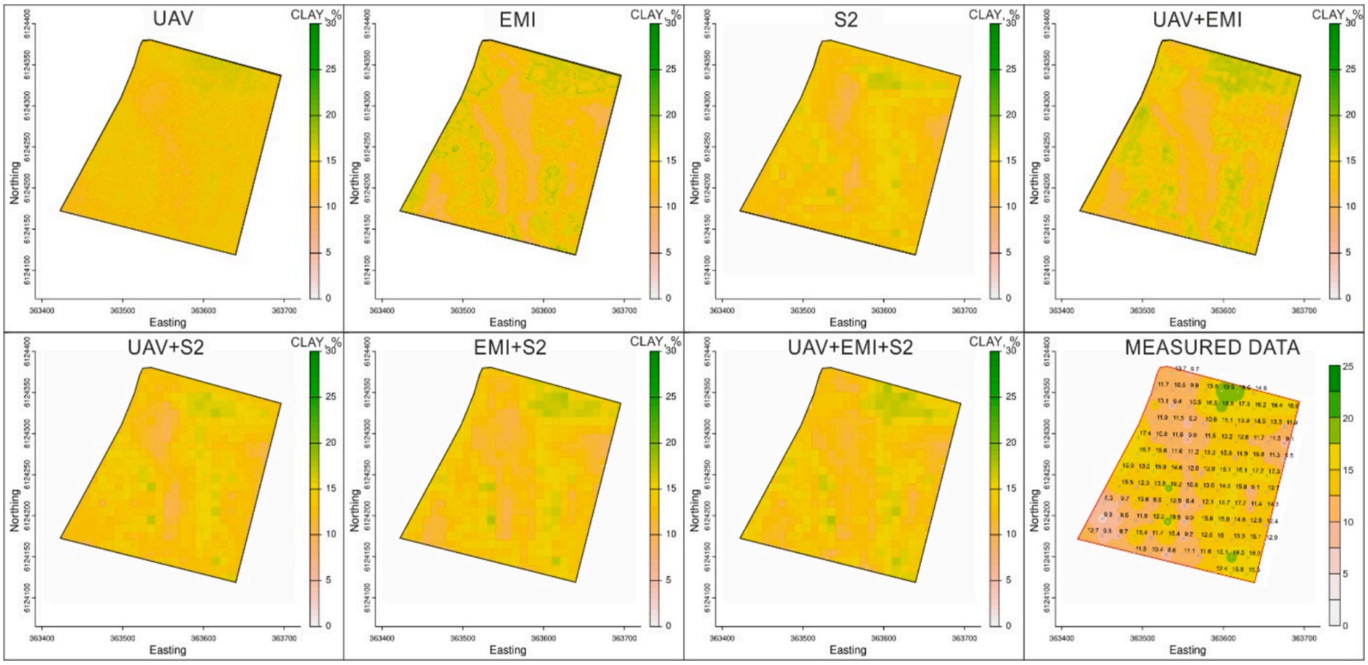

Fig. 11. Clay particle maps for the LT_LYD field and all modelling scenarios, along with the interpolated measured data (bottom right). The axes represent coordinates in the Universal Transverse Mercator (UTM) system.

influenced by the different resolutions of the modelling scenarios rather than variations in prediction accuracy.

In the LT_LYD field, the SOC and clay was not as strongly correlated ($R2 = 0.18$). This is likely influenced not only by the field's high erosion risk but also by its more complex surface topography and genesis, as it was shaped by glacigenic processes. Although all modelling scenarios successfully captured the slope running through the centre of the field (Fig. 11), their accuracy varied. The R^2 values ranged from 0.34 to 0.56, while RMSE values ranged from 2.3% to 3.0%. In many cases, combining different covariates led to visually improved results, as observed in the UAV + Sentinel-2, UAV + EMI, and UAV + EMI + Sentinel-2 scenarios.

3.5. Sampling reduction: effects on accuracy and costs

In this final section, we analyze how the reduction of the number of soil samples – using only 75, 50, and 25% of the collected samples per field – impacts model accuracy and economic efficiency in soil property predictions. Again, we focus only on SOC and clay, as their models demonstrated the highest prediction accuracy. We slightly modified our modelling approach by performing 100 simulations for each data reduction scenario, randomly partitioning data into training and validation subsets for each iteration, allowing us to calculate both mean accuracy metrics and their associated standard deviations. We selected two indicators to evaluate model accuracy: RMSE and the additionally calculated NRMSE. We retained RMSE because it directly reflects the absolute prediction error, independently of data distribution or mean values, which is particularly important when significantly reducing the amount of data used in the model. Additionally, NRMSE was introduced to facilitate error interpretation in percentage terms, allowing clearer definition of thresholds for prediction acceptability.

Overall, mean RMSE values across different modelling scenarios showed only minor fluctuations as the quantity of data used for prediction was reduced, indicating a moderate impact of data reduction on SOC prediction accuracy (Fig. 12). For instance, in LT_RUM, LT_VIE, and LT_VEZ the mean RMSE (across all seven modelling scenarios) was 0.2, while in LT_LYD it varied from 0.3 to 0.4, and in LT_VAL it varied from 0.1 to 0.2. Although, the mean RMSE showed minimal variation, the standard deviation generally increased with reduced datasets, suggesting higher prediction uncertainty at lower sampling densities. Notably, reducing data usage from 100 to 25% will substantially decrease chemical analysis costs per hectare, while prediction accuracy (as indicated by RMSE and NRMSE values) remained relatively stable. This highlights potential cost-efficiency benefits from adopting reduced sampling and data collection strategies. For example, using 100% of the collected data resulted in SOC determination costs between 240 and 270 EUR per ha, whereas employing only 25% of collected data reduced these costs substantially, down to approximately 60–68 EUR per ha.

Mean RMSE values across different modelling scenarios exhibited slightly higher fluctuations for clay compared to SOC, as the amount of data used for prediction decreased (Fig. 13). For example, mean RMSE ranged from 4.1 to 4.3 in LT_RUM, 3.0–3.3 in LT_VIE, 1.8–2.1 in LT_VEZ, 2.5–2.8 in LT_LYD, and 2.0–2.4 in LT_VAL. As observed for SOC, standard deviations generally increased with reduced data volumes, indicating greater prediction uncertainty. Reducing data usage from 100 to 25% notably decreased analysis costs per hectare while only slightly compromising predictive accuracy (RMSE, NRMSE). For instance, soil texture analysis costs declined substantially from 573 to 648 per ha at full data usage to approximately 143–162 per ha at 25% data usage, emphasizing substantial potential cost-efficiency gains.

It is important to note that the cost-effectiveness evaluation in this study considered only the prices of laboratory analyses for SOC and soil texture, based on actual costs at the time of sampling and analysis in 2021. Costs related to UAV flights, proximal sensor mapping (e.g., EMI), or modelling services were not included, as these services are currently not commercially available to farmers in Lithuania. Therefore, the actual cost of replicating the full data acquisition and modelling

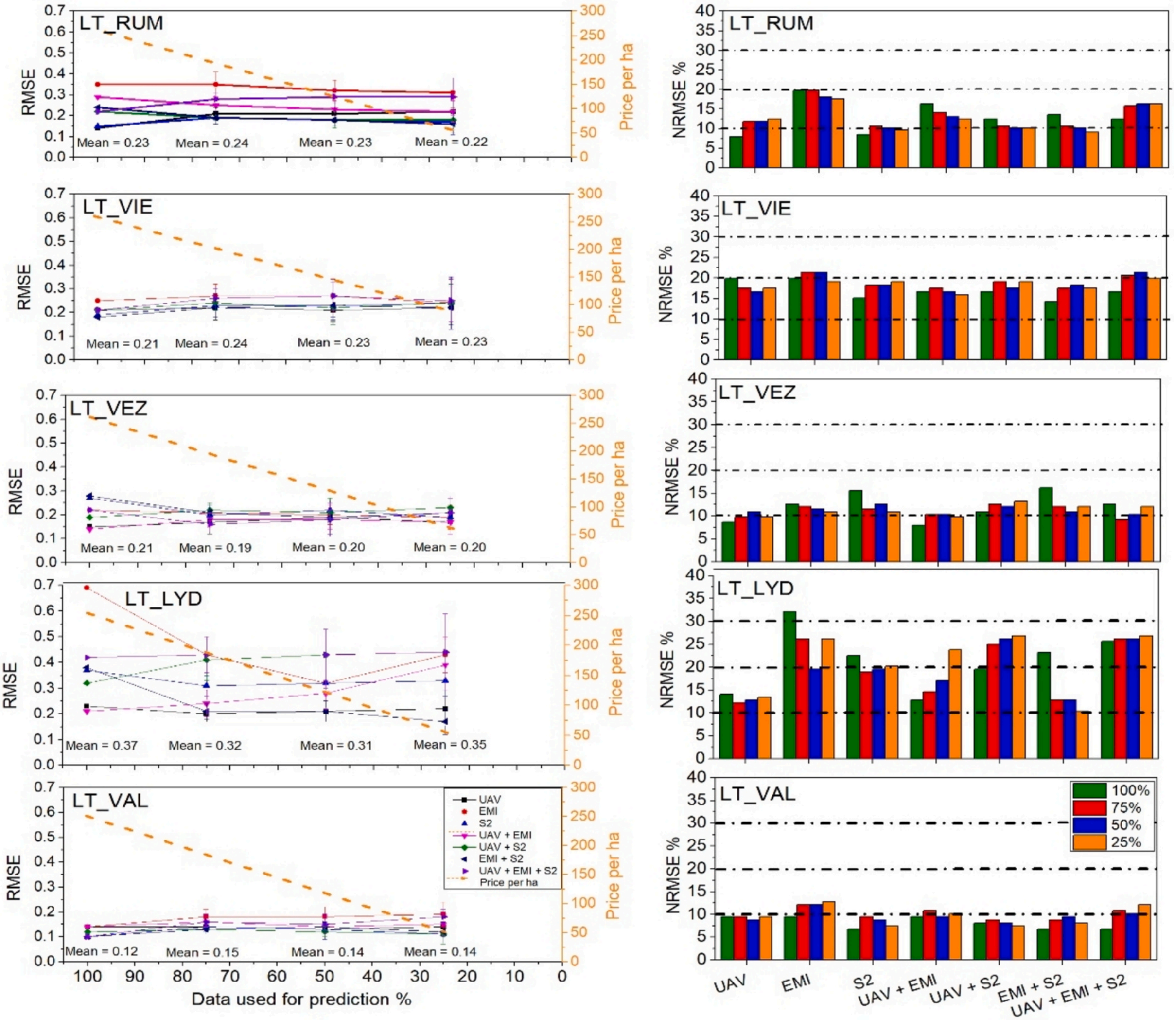

Fig. 12. Impact of three soil data reduction scenarios (25, 50, 75%) on SOC prediction accuracy under different modelling scenarios. Left panels illustrate the mean RMSE with standard deviation and associated changes in the analysis price per hectare as the amount of data used is reduced. Right panels present corresponding NRMSE values, with black threshold lines indicating prediction quality classes: <10% – excellent, 10–20% – good, 20–30% – acceptable, and >30% – poor.

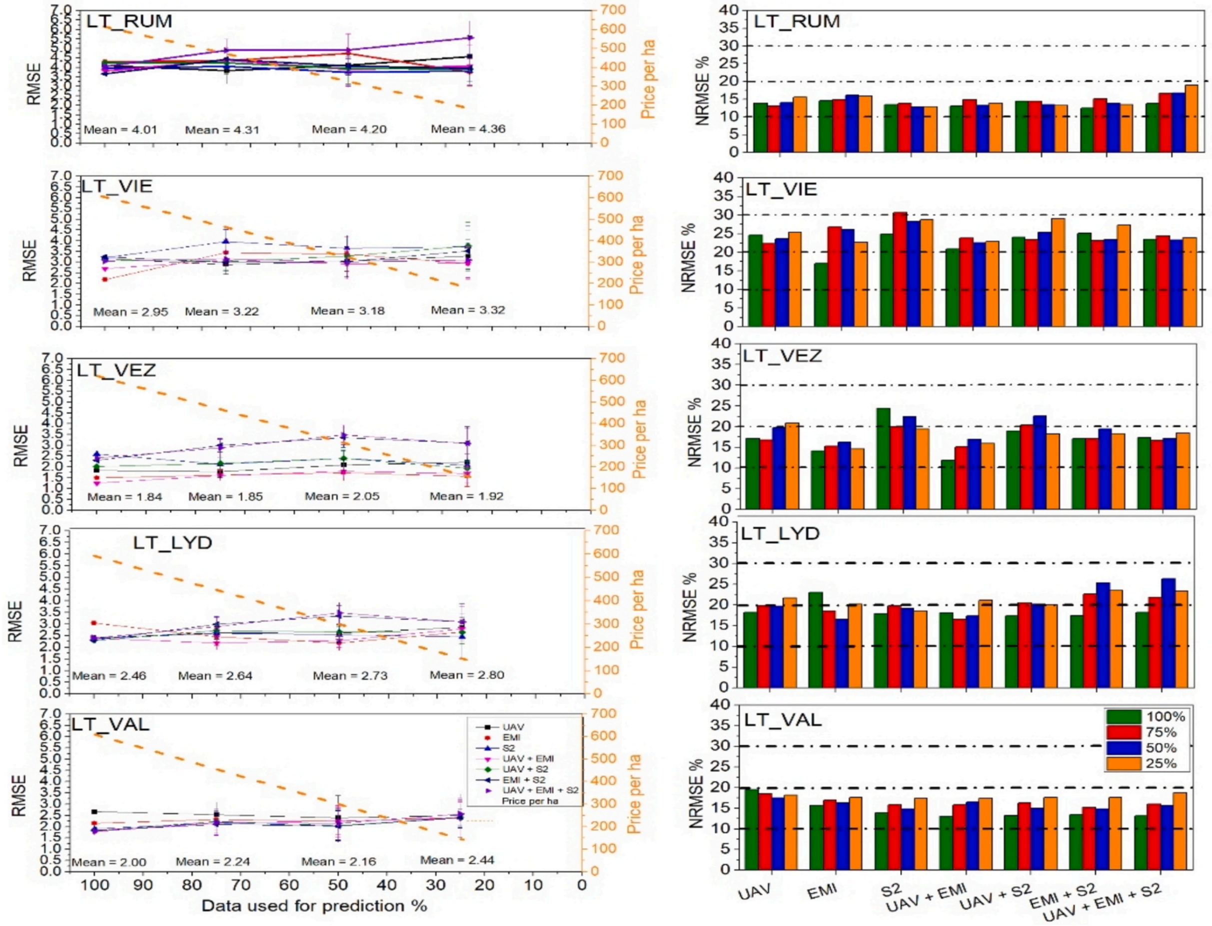

Fig. 13. Impact of three soil data reduction scenarios (25%, 50%, 75%) on Clay prediction accuracy under different modelling scenarios. Left panels illustrate the mean RMSE with standard deviation and associated changes in the analysis price per hectare as the amount of data used is reduced. Right panels present corresponding NRMSE values, with black threshold lines indicating prediction quality classes: <10% – excellent, 10–20% – good, 20–30% – acceptable, and >30% – poor.

workflow presented here would likely be higher. Farmers aiming to obtain similarly detailed soil property maps would need to contract specialized service providers, which could potentially double the total cost compared to the estimates presented in this study.

3.6. Synthesis of findings and practical implications

This study’s novelty lies in integrating high-resolution UAV multispectral imagery with Sentinel-2 satellite data and EMI measurements to predict soil properties, offering a multi-scale perspective not previously explored in the Nordic-Baltic region. Strengths of this study include: (i) the integrated multi-sensor and multi-resolution design combining UAV, Sentinel-2, and EMI data under comparable field-scale conditions; (ii) a high spatial soil sampling density (22–25 samples per hectare), exceeding common farmer practice and enabling robust within-field analysis; (iii) an explicit evaluation of cost–accuracy trade-offs relevant for operational soil mapping; (iv) the use of interpretable machine learning through variable importance (VIP) analysis to link model performance with soil processes; and (v) transparent reporting of both strong and weak predictive results, including cases where multi-sensor fusion did not improve validation performance.

Model performance varied markedly between sites, confirming earlier findings that prediction accuracy is highly site-specific (Wetterlind et al., 2025). This variability aligns with trends reported by Castaldi et al. (2023) and Wetterlind et al. (2025), who noted that local factors – such as climate, soil type, and management – can cause substantial differences in model success across agricultural fields.

Our predictions were based on single-date data collected under specific field conditions (bare soil post-harvest or pre-crop). While bare soil was needed to isolate reflectance, this limits the generalizability of our results to that point in time. Differences in soil water content, surface roughness, or residue cover on the image date will likely influence the model accuracy. Using only one acquisition per site, rather than multi-temporal composites, may reduce consistency, as suboptimal conditions can weaken spectral–soil property relationships at a specific date and as performance varies according to date (Vaudour et al., 2019; Dvorakova et al., 2021; Gomez et al., 2022). This reliance on single-date imagery also limits direct comparability with multi-temporal studies, where temporal compositing can reduce noise related to transient surface and moisture conditions. Although multi-date bare-soil composites can improve robustness, this approach was not feasible in the present study. Only a limited number of Sentinel-2 images met the strict criteria of both bare soil and cloud-free conditions. Using images acquired on different dates or years would have introduced temporal mismatches between soil sampling and images acquisition, meaning that soil moisture, residue cover, and surface conditions at the time of imaging would no longer correspond to those during soil sampling, thereby confounding model calibration. Our goal was also to assess model performance under realistic conditions, where typically only one suitable bare-soil image is available. Therefore, we used single-date imagery matched to the sampling date.

Our findings highlight the importance of spatial resolution and modeling choices in prediction accuracy. UAV imagery captured fine-scale field variability, Sentinel-2 offered broader coverage, and EMI added subsurface conductivity data – each contributing differently to the soil property predictions. Spatial resolution was especially critical: UAV and Sentinel-2 data performed best for SOC, while EMI alone was less effective. The stronger performance of UAV and Sentinel-2 for SOC prediction can be attributed to their sensitivity to surface reflectance in the visible and near-infrared regions, which responds to soil organic matter content, soil colour, and surface roughness. In contrast, EMI integrates bulk subsurface electrical properties that are only indirectly related to SOC. Conversely, EMI substantially improved clay content predictions, reflecting the strong control of clay mineralogy and associated pore water on apparent electrical conductivity. These contrasting sensor responses explain the observed soil-property-specific performance across different sites and indicate that sensor selection should be soil-property-specific, with UAV or Sentinel-2 data preferred for SOC mapping, EMI for texture-related properties, and multi-sensor fusion applied cautiously unless spatial scale and acquisition timing are harmonised.

Poor pH prediction performance illustrates the limitations of sensor-based approaches for soil properties that lack a direct spectral or geophysical response. At the field scale, soil pH exhibits limited sensitivity to spectral reflectance and apparent electrical conductivity, except in cases where carbonates occur in shallow soil layers, as observed at the LT_LYD site. Consequently, pH predictions remained weak regardless of sensor type or combination. Modelling choices also influenced the outcomes, as sensor fusion did not consistently enhance validation performance and, in some cases, led to overfitting. This effect is likely related to the resampling of all predictor layers to the coarsest spatial resolution, which may have reduced the informational value of high-resolution UAV data. Consequently, the potential advantages of multi-sensor combinations were not always translated into improved validation accuracy. Although the soil sampling density was high at the field scale, model uncertainty may still arise from the limited spatial extent of individual fields, as random forest models are sensitive to the structure and representativeness of the training data (Belgiu and Drăguţ, 2016). In addition, the regular 20 × 20 m sampling grid may introduce spatial autocorrelation between training and validation samples. When random data partitioning is applied, this spatial dependence can lead to optimistic validation metrics and should therefore be considered when interpreting model performance.

These results stress the need for careful model calibration, validation strategy, and data integration to achieve reliable predictions.

Finally, a critical reflection on the practical utility of UAV-based multispectral sensing is needed. While UAVs provided detailed soil property maps under ideal conditions, the benefits must be weighed against efforts and costs involved. UAV surveys require specific timing (bare soils) and technical resources, and unlike satellites, there is no broad commercial service offering rapid UAV soil mapping at field scale. In our case, UAVs only marginally improved certain property predictions compared to freely available Sentinel-2 data, raising concerns about cost-effectiveness; however, UAV remain highly valuable for research purposes, model calibration and validation, and the generation of high-resolution baseline datasets. The per-hectare cost of UAV imaging is often much higher than satellite data (Sozzi et al., 2021), making it difficult to justify for large areas. Moreover, models developed at one site were not easily transferable to others, reflecting generalizability issues also noted in other multi-site studies. Given these limitations – such as the need for dry bare fields, limited service availability, and site-specific model tuning – the UAV approach may be more suitable for targeted research applications and site-specific high-resolution assessments, rather than routine mapping. In many cases, satellite imagery (augmented by proximal data like EMI) could offer similar predictive performance, making UAV-based sensing an expensive addition with diminishing returns. Thus, while UAV sensing offers valuable fine-scale insights, its adoption should be critically assessed against its logistical constraints and marginal gains in accuracy. Given the field-scale focus of this study, the developed models were intentionally site-specific, and their transferability across fields with contrasting pedoclimatic conditions is expected to be limited, particularly for SOC and soil water content.

4. Conclusions

This study evaluates the potential of remote sensing and proximal data for mapping six key soil properties – SOC, clay, sand, silt, pH, and soil water content – across five study sites in different agroclimatic zones of Lithuania. Seven modelling scenarios were tested using UAV, Sentinel-2, and EMI data, both individually and in combination, employing a random forest model.

Summarizing the results across all study sites and modelling scenarios, SOC and clay prediction achieved the highest accuracy, while silt, sand, and soil water content predictions posed challenges and demonstrated acceptable accuracy only in specific fields or under certain modelling conditions. Soil pH prediction was generally poor across all scenarios, indicating that pH variations are difficult to capture using the tested remote sensing and proximal sensing approaches. The overall ranking of soil property prediction accuracy is as follows: SOC $\approx$ Clay $>$ Sand $\approx$ Silt $\approx$ SWC $>$ pH. Given the field-scale focus of this study, the developed models are inherently site-specific, and their transferability across fields with contrasting pedoclimatic conditions is expected to be limited.

The effectiveness of different modelling scenarios for soil property prediction varied between fields, suggesting that site-specific natural environmental covariates, such as climate (temperature, rainfall), parent materials, and topography (slope, elevation, etc.), as well as anthropogenic factors like agricultural management, although not explicitly evaluated, likely influenced the predictions across different study sites. It is evident that when predicting soil properties using different sensors and their combinations, the spatial resolution plays a crucial role in the prediction accuracy. In this study, three different resolutions were used – 2.6 cm per pixel, 1 m per pixel, and 10 m per pixel – depending on the type of aerial and proximal data collected. Despite these variations, the results indicate that for SOC prediction, UAV and Sentinel-2 data provided the most accurate results, while EMI alone performed poorly. When combining different sensors for SOC prediction, the predictive power fluctuated without a clear pattern, suggesting that the effectiveness of sensor fusion depends on site-specific conditions; the lack of clear pattern may also be related to resampling all predictors to the coarsest spatial resolution and the associated loss of spectral information from high-resolution UAV data. In contrast, for clay prediction, the inclusion of EMI data led to the most accurate predictions, highlighting the relevance of electrical conductivity measurements for soil texture (especially clay) assessment. Combining multiple sensors generally did not consistently enhance validation accuracy, indicating potential overfitting or site-specific variability in prediction performance, and highlighting the need for cautious interpretation of apparent training gains in multi-sensor soil property modelling. Model performance should be interpreted in the context of single-date bare-soil imagery, which reflects realistic conditions but limits direct comparison with multi-temporal studies.

CRediT authorship contribution statement

R. Žydelis: Writing – review & editing, Writing – original draft, Visualization, Methodology, Investigation, Formal analysis, Data curation, Conceptualization, Funding acquisition, Project administration, Supervision. **L. Weihermüller:** Writing – review & editing, Writing – original draft. **L.C. Gomes:** Writing – review & editing. **A.B. Møller:** Writing – review & editing, Investigation, Data curation. **F. Castaldi:** Writing – review & editing, Methodology, Conceptualization, Writing – original draft. **J. Volungevičius:** Writing – review & editing, Visualization, Investigation, Data curation. **A. Kavaliauskas:** Writing – review & editing, Software, Investigation, Formal analysis, Data curation. **T.**

Koganti: Writing – review & editing, Formal analysis, Data curation. **J. Wetterlind:** Writing – review & editing, Conceptualization, Funding acquisition, Supervision. **İ. Cinkaya:** Writing – review & editing. **L. Borůvka:** Writing – review & editing. **F. van Egmond:** Writing – review & editing. **S. Higgins:** Writing – review & editing. **F. Liebisch:** Writing – review & editing. **V. Povilaitis:** Writing – review & editing, Investigation. **A. Kazlauskaitė-Jadzevičė:** Writing – review & editing. **K. Amalevičiūtė-Volungė:** Writing – review & editing, Investigation. **S. Pranaitienė:** Writing – review & editing, Investigation. **E. Vaudour:** Conceptualization, Funding acquisition, Methodology, Supervision, Writing – original draft.

Funding

Soil samples, remote sensing, and proximal data were collected as part of the STEROPES and SensRes projects (https://ejpsoil.eu/soil-research/STEROPES), within the EJP SOIL program, funded by the European Union's Horizon 2020 research and innovation program (grant agreement No. 862695) and by the participating Member States. The modeling component of this study was conducted as part of the “Sensor data for Enhanced soil properties prediction in Lithuanian Agroclimatic zones” (AgroSens) project, funded by the Research Council of Lithuania (LMTLT) under agreement No. S-MIP-24-106.

Declaration of competing interest

The authors declare that they have no known competing financial interests or personal relationships that could have appeared to influence the work reported in this paper.

Appendix A. Supplementary data

Supplementary data to this article can be found online at https://doi.org/10.1016/j.compag.2026.111543.

Data availability

Data will be made available on request.

References

Adhikari, K., Hartemink, A.E., 2016. Linking soils to ecosystem services – a global review. Geoderma 262, 101–111. https://doi.org/10.1016/j.geoderma.2015.08.009.

Aqdam, K.K., Mahabadi, N.Y., Ramezanpour, H., Rezapour, S., Mosleh, Z., Zare, E., 2022. Comparison of the uncertainty of soil organic carbon stocks in different land uses. J. Arid Environ. 205, 104805. https://doi.org/10.1016/j.jaridenv.2022.104805.

Auken, E., Viezzoli, A., Christensen, A., 2009. A single software for processing, inversion, and presentation of AEM data of different systems: the Aarhus Workbench. ASEG Ext. Abstract 1, 1–5. https://doi.org/10.1071/ASEG2009ab062.

Auken, E., Christiansen, A.V., Kirkegaard, C., Fiandaca, G., Schamper, C., Behroozmand, A.A., Binley, A., Nielsen, E., Effersø, F., Christensen, N.B., Sørensen, K., Foged, N., Vignoli, G., 2015. An overview of a highly versatile forward and stable inverse algorithm for airborne, ground-based and borehole electromagnetic and electric data. Explor. Geophys. 46 (3), 223–235. https://doi.org/10.1071/EG13097.

Babaeian, E., Sidike, P., Newcomb, M.S., Maimaitijiang, M., White, S., Demieville, J., Ward, R.W., Sadeghi, M., LeBauer, D.S., Jones, S.B., Sagan, V., Tuller, M., 2019. A new optical remote sensing technique for high-resolution mapping of soil moisture. Front. Big Data 2, 37. https://doi.org/10.3389/fdata.2019.00037.

Basalykas, A. 2014. Lietuvos kraštovaizdis (In Lithuanian). Vilniaus universitetas.

Belgiu, M., Drăguţ, L., 2016. Random forest in remote sensing: a review of applications and future directions. ISPRS J. Photogramm. Remote Sens. 114, 24–31. https://doi.org/10.1016/j.isprsjprs.2016.01.011.

Benedetto, D.D., Barca, E., Castellini, M., Popolizio, S., Lacolla, G., Stellaci, A.M., 2022. Prediction of soil organic carbon at field scale by regression kriging and multivariate adaptive regression splines using geophysical covariates. Land 11 (3), 381. https://doi.org/10.3390/land11030381.

Biney, J.K.M., Houška, J., Volánek, J., Abebrese, D.K., Cervenka, A., 2023. Examining the influence of bare soil UAV imagery combined with auxilliary datasets to estimate and map soil organic carbon distribution in an erosion-prone agricultural field. Sci. Total Environ. 870, 161973. https://doi.org/10.1016/j.scitotenv.2023.161973.

Bouslihim, Y., John, K., Miftah, A., Azmi, R., Aboutayeb, R., Bouasria, A., Razouk, R., Hssaini, L., 2024. The effect of covariates on Soil Organic Matter and pH variability: a digital soilmapping approach using random forest model. Ann. GIS 30 (2), 215–232.

Brogi, C., Huisman, J.A., Herbst, M., Weihermüller, L., Klosterhalfen, A., Montzka, C., Reichenau, T.G., Vereecken, H., 2020. Simulation of spatial variability in crop leaf index and yield using agroecosystem modeling and geophysics-based quantitative soil information. Vadose Zone J. 19 (1), e20009. https://doi.org/10.1002/vzj2.20009.

Brogi, C., Huisman, J.A., Weihermüller, L., Herbst, M., Vereecken, H., 2021. Added value of geophysics in agro-ecosystem simulations. Soil 7, 125–143. https://doi.org/10.5194/soil-7-125-2021.

Bukantis, 2009. Agroclimatic Zoning. Lithuanian National Atlas. National Land Service under the Ministry of Agriculture, Vilnius.

Castaldi, F., Halil Koparan, M., Wetterlind, J., Žydelis, R., Vinci, I., Savaş, A.Ö., Kivrak, C., Tunçay, T., Volungevičius, J., Obber, S., Ragazzi, F., Malo, D., Vaudour, E., 2023. Assessing the capability of Sentinel-2 time-series to estimate soil organic carbon and clay content at local scale in croplands. ISPRS J. Photogramm. Remote Sens. 199, 40–60. https://doi.org/10.1016/j.isprsjprs.2023.03.016.

Castaldi, F., 2021. Sentinel-2 and landsat-8 multi-temporal series to estimate topsoil properties on croplands. Remote Sens. (Basel) 13 (17), 3345. https://doi.org/10.3390/rs13173345.

Castaldi, F., Chabrillat, S., Don, A., Wesemael, B.V., 2019. Soil organic carbon mapping using LUCAS topsoil database and sentinel-2 data: an approach to reduce soil moisture and crop residue effects. Remote Sens. (Basel) 11 (18), 2121. https://doi.org/10.3390/rs11182121.

Chen, P.Y., Chen, C.C., Kang, C., Liu, J.W., Li, Y.H., 2025. Soil water content prediction across seasons using random forest based on precipitation-related data. Comput. Electron. Agric. 230, 109802. https://doi.org/10.1016/j.compag.2024.109802.

Christiansen, A.V., Pedersen., J.B., Auken, E., Søe, N.E., Holst, M. J., Kristiansen, S.M., 2016. Improved geoarchaeological mapping with electromagnetic induction instruments from dedicated processing and inversion. Remote Sens. (Basel) 8 (12), 1022. https://doi.org/10.3390/rs8121022.

Dvorakova, K., Heiden, U., Staats, G., Van Os, G., van Wesemael, B., 2023. Improving soil organic carbon predictions from a Sentinel-2 soil composite by assessing surface conditions and uncertainties. Geoderma 429, 116128. https://doi.org/10.1016/j.geoderma.2022.116128.

Dvorakova, K., Heiden, U., van Wesemael, B., 2021. Sentinel-2 exposed soil composite for soil organic carbon prediction. Remote Sens. (Basel) 13 (9), 1791. https://doi.org/10.3390/rs13091791.

EU, Soil health : reaping the benefits of healthy soils, for food, people, nature and the climate, Publications Office, 2021, https://data.europa.eu/doi/10.2830/057952.

Faramarzi, S.E., Pazira, E., Masihabadi, M.H., Torkashvand, A.M., Motamedvaziri, B., 2022. Modeling and estimating the spatial distribution of soil organic matter content in irrigated lands.International. J. Environ. Sci. Technol. 19, 7399–7410. https://doi.org/10.1007/s13762-022-03909-2.

Gholizadeh, A., Žižala, D., Saberioon, M., Borůvka, L., 2018. Soil organic carbon and texture retrieving and mapping using proximal, airborne and Sentinel-2 spectral imaging. Remote Sens. Environ. 218, 89–103. https://doi.org/10.1016/j.rse.2018.09.015.

Gogumalla, P., Rupavatharam, S., Datta, A., Khopade, R., Choudhari, P., Dhulipala, R., Dixit, S., 2022. Detecting soil pH from open-source remote sensing data: a case study of Angul and Balangir Districts, Odisha State. J. Indian Soc. Remote Sens. 50, 1275–1290. https://doi.org/10.1007/s12524-022-01524-9.

Gomez, C., Vaudour, E., Féret, J.B., de Boissieu, F., Dharumarajan, D., 2022. Topsoil clay content mapping in croplands from Sentinel-2 data: Influence of atmospheric correction methods across a season time series. Geoderma 423, 115959. https://doi.org/10.1016/j.geoderma.2022.115959.

Gomes, L.C., Beucher, A.M., Møller, A.B., Iversen, B.V., Børgesen, C.D., Adetsu, D.V., Sechu, G.L., Heckrath, G.J., Koch, J., Adhikari, K., et al., 2023. Soil assessment in Denmark: towards soil functional mapping and beyond. Front. Soil Sci. 3, 1090145. https://doi.org/10.3389/fsoil.2023.1090145.

Han, Y.S., Fillippi, P., Singh, K., Whelan, B.M., Bishop, T.F.A., 2022. Assessment of global, national and regional-level digital soil mapping products at different spatial supports. Eur. J. Soil Sci. 73 (5), e13300. https://doi.org/10.1111/ejss.13300.

Hartemink, A.E., Barrow, N.J., 2023. Soil pH - nutrient relationships: the diagram. Plant and Soil 486, 209–215. https://doi.org/10.1007/s11104-022-05861-z.

Hegazi, E.H., Samak, A.A., Yang, L., Huang, R., Huang, J., 2023. Prediction of soil moisture content from sentinel-2 images using convolutional neural network (CNN). Agronomy 13, 656. https://doi.org/10.3390/agronomy13030656.

Hiemstra, P and Skoien, J.O. 2025. Automatic interpolation Package. Version: 1.1-16. https://cran.r-project.org/web/packages/automap/index.html (accessed 2025-05-09).

Kaufmann, M.S., von Hebel, C., Weihermüller, L., Baumecker, M., Döring, T., Schweitzer, K., Hobley, E., Bauke, S.L., Amelung, W., Vereecken, H., van der Kruk, J., 2019. Effect of fertilizers and irrigation on multi-configuration electromagnetic induction measurements. Soil Use Manag. 36 (1), 104–116. https://doi.org/10.1111/sum.12530.

Kavaliauskas, A., Žydelis, R., Castaldi, F., Auškalnienė, O., Povilaitis, V., 2023. Predicting maize theoretical methane yield in combination with ground and UAV remote data using machine learning. Plants 12 (9), 1823. https://doi.org/10.3390/plants12091823.

Kibblewhite, M.G., Ritz, K., Swift, M.J., 2007. Soil health in agricultural systems. Philos. Trans. R. Soc. B 363, 1492. https://doi.org/10.1098/rstb.2007.2178.

Kuhn, M., 2008. Building predictive models in R using the caret package. J. Statist. Softw. 28 (5), 1–26. https://doi.org/10.18637/jss.v028.i05.

Lamichhane, S., Kumar, L., Wilson, B., 2019. Digital soil mapping algorithms and covariates for soil organic carbon mapping and their implications: a review. Geoderma 352, 395–413. https://doi.org/10.1016/j.geoderma.2019.05.031.

Lemercier, B., Lagacherie, P., Amelin, J., Sauter, J., Pichelin, P., Richer-de-Forges, A.C., Arrouays, D., 2022. Multiscale evaluations of global, national and regional digital soil mapping products in France. Geoderma 425 (1), 116052. https://doi.org/10.1016/j.geoderma.2022.116052.

Leifeld, J., 2023. Carbon farming: climate change mitigation via non-permanent carbon sinks. J. Environ. Manage. 33, 117893. https://doi.org/10.1016/j.jenvman.2023.117893.

Mahmood, H.S., Hoogmoed, W.B., van Henten, E.J., 2012. Sensor data fusion to predict multiple soil properties. Precis. Agric. 13, 628–645. https://doi.org/10.1007/s11119-012-9280-7.

McBratney, A.B., Mendonca Santos, M.L., Minasny, B., 2003. On digital soil mapping. Geoderma 117 (1–2), 3–52. https://doi.org/10.1016/S0016-7061(03)00223-4.

Mgohele, R.N., Massawe, B.H.J., Shitindi, M.J., Sanga, H.G., Omar, M.M., 2024. Prediction of soil texture using remote sensing data. a systematic review. Front. Remote Sens. 5, 1461537. https://doi.org/10.3389/frsen.2024.1461537.

Metzger, M.J., Shkaruba, A.D., Jongman, R. H.G., Brunce, R. G.H. 2012. Description of the European environmental zones and strata. Alterra Report 2281. Wageningen, 154, pp.

Mendes, J.A.J., Carvalho, N.G.P., Mourarias, M.N., Careta, C.B., Zuin, V.G., Gerolama, 2022. Dimensions of digital transformation in the context of modern agriculture. Sustainable Prod. Consumption 34, 613–637. https://doi.org/10.1016/j.spc.2022.09.027.

Mohsan, S.A.H., Khan, M.A., Noor, F., Ullah, I., Alsharif, M.H., 2022. Drones 6 (6), 147. https://doi.org/10.3390/drones6060147.

Moriasi, D.N., Arnold, J.G., Van Liew, M.W., Binger, R.L., Harmel, R.D., Veith, T.L., 2007. Model evaluation guidelines for systematic quantification of accuracy in watershed simulations. Trans. ASABE 50 (3), 885–900. https://doi.org/10.13031/2013.23153.

Møller, A.B., Koganti, T., Beucher, A., Iversen, B.V., 2021. Downscaling digital soil maps using electromagnetic induction and aerial imagery. Geoderma 385 (1), 114852. https://doi.org/10.1016/j.geoderma.2020.114852.

National paying agency. Spatial crop declaration data set of the territory of the Republic of Lithuania at scale 1:10 000. 2023. https://www.geoportal.lt/metadata-catalog/catalog/search/resource/details.page?uuid=%7B7AF3F5B2-662.

Richer-de-Forges, A.C., Chen, Q., Baghdadi, N., Chen, S., Gomez, C., Jacquemoud, S., Martelet, G., Mulder, V.L., Urbina-Salazar, D., Voudour, E., Weiss, M., Wigneron, J. P., Arrouays, D., 2023. Remote sensing for digital soil mapping in french research – a review. Remote Sens. (Basel) 15, 3070. https://doi.org/10.3390/rs15123070.

Mgohele, R.N., Massawe, B.H.J., Shitindi, M.J., Sanga, H.G., Omar, M.M., 2024. Prediction of soil texture using remote sensing data. a systematic review. Front. Remote Sens. 5, 1461537. https://doi.org/10.3389/frsen.2024.1461537.

Schmäck, J., Weihermüller, L., Klotzsche, A., von Hebel, C., Pätzold, S., Welp, G., Vereecken, H., 2021. Large-scale detection and quantification of harmful soil compaction in a post-mining landscape using multi-configuration electromagnetic induction. Soil Use Manag. 38 (1), 212–228. https://doi.org/10.1111/sum.12763.

Segarra, J., Buchaillot, M.L., Araus, J.L., Kefauver, S.C., 2022. Remote sensing for precise agriculture: sentinel-2 improved features and applications. Agronomy 10 (5), 641. https://doi.org/10.3390/agronomy10050641.

Sozzi, M., Kayad, A., Gobbo, S., Cogato, A., Sartori, L., Marinello, F., 2021. Economic comparison of satellite, plane and UAV-acquired NDVI images for site-specific nitroge application: observations from Italy. Agronomy 11 (11), 2098. https://doi.org/10.3390/agronomy11112098.

Stenberg, B., Viscarra Rossel, R.A., Mouazen, A.M., Wetterlind, J., 2010. Chapter five - Visible and Near Infrared Spectroscopy in Soil Science. Adv. Agron. 107, 163–215. https://doi.org/10.1016/S0065-2113(10)07005-7.

Söderström, M., Sohlenius, G., Rodhe, L., 2016. Adaptation of regional digital soil mapping for precision agriculture. Precis. Agric. 17, 588–607. https://doi.org/10.1007/s11119-016-9439-8.

Taylor, R. 2011. Introducing Dualem to the IUSS working group on proximal soil sensing. Dualem Inc., Milton, On, L9T 3A2, Canada.

Tziolas, N., Tsakiridis, N., Chabrillat, S., Demattê, J.A.M., Ben-Dor, E., Gholizadeh, A., Zalidis, G., Wesemael, B.V., 2021. Earth observation data-driven cropland soil monitoring: a review. Remote Sens. (Basel) 13 (21), 4439. https://doi.org/10.3390/rs13214439.

Urbina-Salazar, D., Vaudour, E., Richer-de-Forges, A.C., Chen, S., Martelet, G., Baghdadi, N., Arrouays, D., 2023. Sentinel-2 and Sentinel-1 bare soil temporal mosaics of 6-year periods for soil organic carbon content mapping in Central France. Remote Sens. (Basel) 15, 2410. https://doi.org/10.3390/rs15092410.

Vanongeval, F., van Orshoven, J., Gobin, A. Contribution of Sentinel-2 spring seedbed spectra to the digital mapping of soil organic carbon concentration. Geoderma, 449: 116984. doi: 10.1016/j.geoderma.2024.116984.

Vaudour, E., Gholizadeh, A., Castaldi, F., Saberioon, M., Borůvka, L., Urbina-Salazar, D., Fouad, Y., Arrouays, D., Richer-de-Forges, A.C., Biney, J., Wetterlind, J., Van Wesemael, B., 2022. Satellite imagery to map topsoil organic carbon content over cultivated areas: an overview. Remote Sens. (Basel) 14 (12), 2917. https://doi.org/10.3390/rs14122917.

Vaudour, E., Gomez, C., Loiseau, T., Baghdadi, N., Loubet, B., Arrouays, D., Ali, L., Lagacherie, P., 2019. The impact of acquisition date on the prediction performance of topsoil organic carbon from sentinel-2 for croplands. Remote Sesns. 11 (18), 2143. https://doi.org/10.3390/rs11182143.

Viezzoli, A., Christiansen, A.V., Auken, E., Sørensen, K., 2008. Quasi-3D modeling of airborne TEM data by spatially constrained inversion. Geophysics 73 (3), F105–F113. https://doi.org/10.1190/1.2895521.

Vogel, H.J., Bartke, S., Daedlow, K., Helming, K., Kögel-Knabner, I., Lang, B., Rabot, E., Russell, D., Stößel, B., Weller, U., Wiesmeier, M., Wollschläger, U., 2018. A systemic approach for modeling soil functions. Soil 4, 83–92. https://doi.org/10.5194/soil-4-83-2018.

Wallach, D. (2006). Evaluating crop models. In Wallach D., Makowski D., Jones J.W. (Eds), Working with Dynamic Crop Models, Elsevier, The Netherlands, pp.11−55.

Wetterlind, J., Piikki, K., Stenberg, B., Söderström, M., 2015. Exploaring the predictability of soil texture and organic matter content with a commercial integrated soil profiling tool. Eur. J. Soil Sci. 66 (4), 631–638. https://doi.org/10.1111/ejss.12228.

Wetterlind, J., Simmler, M., Castaldi, F., Borůvka, L., Gabriel, J.L., Gomes, L.C., Khosravi, V., Kivrak, C., Koporan, M.H., Lázaro-López, A., Lopatka, A., Liebisch, F., Rodriguez, J.A., Savas, A.Ö., Stenberg, B., Tuncay, T., Vinci, I., Volungevičius, J., Žydelis, R., Vaudour, E., 2025. Influnece of Soil Texture on the Estimation of Soil Organic Carbon from Sentinel-2 Temporal Mosaics at 34 European Sites. Eur. J. Soil Sci. 76 (1), e70054. https://doi.org/10.1111/ejss.70054.

William, A, J., Wilford, R. G., Walter, H. G. Soil physics. Wiley; 5th edition, 1991.

Volungevicius, J., Žydelis, R., Amaleviciute-Volunge, K., 2024. Advancements in soil organic carbon mapping and interpolation techniques: a case study from Lithuania's Moraine Plains. Sustainability 16, 5157. https://doi.org/10.3390/su16125157.

WRB. 2022. World Reference Base for Soil Resources. International soil classification system for naming soils and creating legends for soil maps. 4th edition. International Union of Soil Sciences (IUSS), Vienna, Austria.

Yuzugullu, O., Fajraoui, N., Don, A., Liebisch, F., 2024. Satellite-based soil organic carbon mapping on European soils using available datasets and support sampling. Sci. Remote Sens., 100118 https://doi.org/10.1016/j.srs.2024.100118.

Zayani, H., Fouad, Y., Michot, D., Kassouk, Z., Baghdadi, N., Vaudour, E., Lili-Chabaane, Z., Walter, C., 2023. Using machine-learning algorithms to predict soil organic carbon content from combined remote sensing imagery and laboratory Vis-NIR spectral datasets. Remote Sens. (Basel) 15 (17), 4264. https://doi.org/10.3390/rs15174264.

Žižala, D., Minařík, R., Zádorová, T., 2019. Soil organic carbon mapping using multispectral remote sensing data: prediction ability of data with different spatial and spectral resolutions. Remote Sens. (Basel) 11 (24), 2947. https://doi.org/10.3390/rs11242947.